TÉCNICO LISBOA

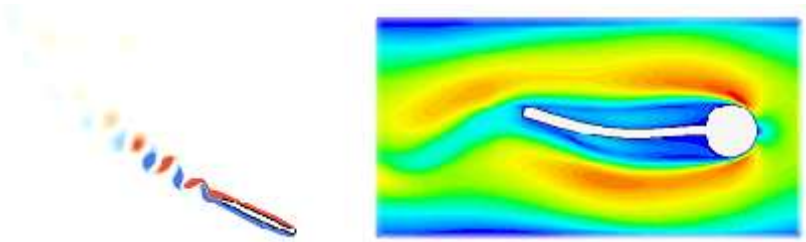

Numerical Study of 2-D Rigid and Deformable Fluid-Structure Interaction Cases

Pedro Carrusca Gomes

Thesis to obtain the Master of Science Degree in

Mechanical Engineering

Supervisor: Prof. José Carlos Fernandes Pereira

Co-Supervisor: Prof. José Manuel da Silva Chaves Ribeiro Pereira

Examination Committee

Chairperson: Prof. Viriato Sérgio de Almeida Semião

Supervisor: Prof. José Carlos Fernandes Pereira

Member of the Committee: Prof. Luís Rego da Cunha de Eça

November 2014

À minha Avó

Resumo

Os efeitos de um escoamento cruzado foram estudados para os regimes de queda livre tumbling e fluttering de uma placa bi-dimensional usando simulação numérica. Foi utilizado o código comercial STAR-CCM+, o procedimento numérico foi previamente verificado e validado.

A análise focou-se em velocidades e forças instantâneas durante períodos típicos (i.e. médios) de cada regime de queda para várias velocidades do escoamento cruzado, também foram analisadas velocidades médias durante a trajectória e o período para analisar os efeitos do escoamento cruzado nos dois regimes.

Obtiveram-se provas significativas que o escoamento cruzado apenas influencia a velocidade horizontal e de forma linear. Uma placa em tumbling ou fluttering com Reynolds médio de queda da ordem de 10^3 comporta-se como uma esfera em escoamento de Stokes.

Foram estudados casos típicos de interacção fluído estrutura recorrendo aos códigos comerciais STAR-CCM+ e ABAQUS em co-simulação. Um caso foi utilizado para verificação enquanto outro, fisicamente mais rico, foi utilizado para estudar fenómenos chave de interacção fluído estrutura.

Aspectos numéricos importantes para a simulação deste tipo de casos são apresentados e os resultados comparados com os obtidos por outros autores.

Palavras chave: Simulação; Numérica; CFD; Queda-livre; FSI.

Abstract

The effects of cross-flow on the tumbling and fluttering motions of a free-falling 2D plate were studied using numerical simulation. The commercial code STAR-CCM+ was used, the numerical procedure was previously verified and validated.

The analysis focused on velocities and forces during typical periods (obtained trough averaging) of each motion at various cross-flow velocities, and also mean velocities during the motion periods and the whole trajectory to conclude how the cross-flow influences the two regimes.

Significant evidence that cross-flow only influences horizontal velocity in a linear fashion was found, a tumbling or fluttering plate falling with average Reynolds of order 10^3 behaves like a sphere falling in Stokes flow.

Elastic-coupling Fluid Structure Interaction benchmark cases were studied using commercial codes STAR-CCM+ and ABAQUS in co-simulation. One case was used for solution verification while another, physically richer, was used to analyze key phenomena in Fluid Structure Interaction.

Numerical aspects important for this kind of simulation are reviewed and the results compared to the ones obtained by other authors.

Keywords: Numerical; Simulation; CFD; Free-fall; FSI.

Acknowledgements

I would like to express my gratitude to Prof. Dr. José Carlos Fernandes Pereira and to Prof. Dr. José Manuel da Silva Chaves Ribeiro Pereira for their guidance and expertise in the supervision of this work.

To the colleague Nicola Zorzi for his help in the initial setup of the simulations.

To the LASEF team in particular Dr. Duarte Albuquerque, Telma Oliveira and Filipe Teixeira for their help in solving software problems.

To IST, specially the LASEF research group for the hardware and software necessary to this work.

Contents

List of Figures

List of Tables

Acronyms

ALE – Arbitrary Lagrangian Eulerian.

CFD – Computational Fluid Dynamics.

DFBI – Dynamic Fluid-Body Interaction.

FEM – Finite Element Method.

FSI – Fluid-Structure Interaction.

FVM – Finite Volume Method.

IIE – Instability Induced Excitation.

LES – Large Eddy Simulation.

MIE – Movement Induced Excitation.

NS – Navier-Stokes equations.

NURBS – Non Uniform Rational B Spline.

SIMPLE – Semi Implicit Method for Pressure Linked Equations.

V&V – Verification and Validation.

2D – Two dimensional.

1 - Introduction

FSI usually refers to cases where a solid and fluid domain interact leading to a coupled system, i.e. the solid's displacement, deformation or both condition the flow around it which in turn alters the forces acting on the solid.
Such cases are widely present in nature, for instance in seed dispersion and fire spreading mechanisms. FSI is also present in man made structures, in such cases it is a large concern for it can (and has) lead do significant disasters, such as the Takoma Narrows bridge or the cooling towers of Ferrybridge “C” power station. There are however systems where significant displacements are desired, ocean energy conversion devices are an example.
With the advances in material science and engineering in general structures are becoming lighter and more flexible, in consequence the resulting systems are more tightly coupled and so the importance of FSI increases along with the difficulty do predict it.
The ability to predict solid-fluid interactions is important as a tool to study nature's mechanisms and to design safe/high performance structures.

1.1 - Motivation

The study of free falling objects is rich from both the numerical and physics point of view. Numerically because it requires strong methods to cope with the tightly coupled systems formed by light and/or compliant solids in heavy liquids (in a relative sense). Physically because of the numerous phenomena influencing the motion, boundary layer separation, vortex-shedding, possibility of the body interacting with its wake directly (by crossing it) to name a few.
Due to the complex phenomena involved even the study of simple objects like plates can offer insight in complex topics like insect flight [Ansari et al. 2006], seed dispersion [McCutchen, 1977], particle sedimentation [Allen, 1984], fire spreading [Sardoy et al. 2007], debris dispersion [Kalimpa et al. 2012] etc.
Fluid-Structure Interaction (FSI) involving deformable structures is perhaps the most important for engineering applications, from civil engineering structures like buildings and bridges, aircraft wings from aeronautic engineering, to submerged pipelines and drills from the oil and gas industry the applications are countless. For biological sciences there is also great interest in studying deformable structures such as the arteries, heart valves, vocal cords, etc (see for instance [Luo et al. 2013]).

1.2 - Objectives

In the first part of this work the effects of cross-flow on the motion regimes tumbling and fluttering are studied, the purpose is to identify changes in the regimes or possible transitions to other regimes. The commercial code STAR-CCM+ was used since it has been showed by other authors [Zorzi, 2013] that

the numerical results obtained are in good agreement with experimental results and numerical results obtained with other codes.

In the second part an elastic-coupling case is studied, the purpose of which is to evaluate the co-simulation capabilities of STAR-CCM+ and ABAQUS in tightly coupled FSI cases, laying the grounds for the simulation of movable deformable structures.

In chapter 2, the mathematical formulation and some numerical aspects of importance when selecting methods and associated parameters are presented. Chapters 3 and 4 are dedicated to each case study, they comprise literature review, verification and validation and the analysis itself. In chapter 5 the conclusions and future work suggestions are presented.

2. Mathematical Formulation and Numerical Methods

This chapter is dedicated to the mathematical models used to model the physics present in the cases studied in this work (fluid flow, rigid body motion and deformation) and to the numerical methods used to solve the equations and to couple their solution in multi-physics problems.

2.1 Mathematical Models

Both in dynamic coupling and elastic coupling the forces acting on the structure are due to the fluid, to determine them the fluid-flow equations need to be solved, in dynamic coupling the structure response to the forces is obtained solving the rigid body dynamics equations whereas in elastic coupling one needs to solve the stress equilibrium equations using the pertinent form of strain-displacement relations and material constitutive law.

2.1.1 Fluid-Flow

The forces acting on the structure (shear and pressure) are determined solving the Navier-Stokes equations and the continuity equation. The cases studied in this thesis are all in the laminar regime and due to the low velocities and the fluid being water the incompressible form of the equations may be used.

$$\nabla . u = 0$$
$$\frac{\partial u}{\partial t} + (u . \nabla) u = -\frac{1}{\rho} \nabla p + \nu \nabla^2 u \quad (1)$$

Where u is the velocity vector, t is time, ρ the fluid density, p pressure and v the kinematic viscosity.
The boundary condition for solid walls is the no-slip condition, which states that the fluid and solid velocities must be equal.

2.1.2 Rigid Body Motion

When the solid is assumed rigid its motion is governed by the 6 equations of motion (which reduce to 3 for 2D cases), Newton's second law:

$$m\, a = F \quad (2)$$

Where “m” is mass, “a” the body's acceleration and “F” the summation of forces. And Euler's equations that in a rotating reference frame with origin in the body's center of mass may be written in vector form as:

$$I\, \dot{\omega} + \omega \times (I\, \omega) = M \quad (3)$$

Where “I” is the tensor of moments of inertia, “ω” the angular velocity vector and “M” the summation of moments about the center of mass.

This is an initial value problem and therefore no boundary conditions exist, both the summation of forces and the summation of moments are obtained integrating the pressure and shear stress over the body's surface.

$$F = \int_A p\, n_s\, dA + \int_A \tau_s\, dA \tag{4}$$

$$M = \int_A p\, r \times n_s\, dA + \int_A r \times \tau_s\, dA \tag{5}$$

Where n_s is the surface normal, τ_s the shear stress on the wall and “r” the distance vector from the center of mass to an arbitrary point in the body's surface.

2.1.3 Deformation

When the solid can't be assumed rigid 3 sets of equations are necessary, the first is the equilibrium of stresses.

$$\nabla \cdot \sigma + f = \rho\, a \tag{6}$$

Where σ is the Cauchy stress tensor, “f” are the volume forces and “a” the acceleration of the material point. In these 3 equations 9 unknowns appear (6 stresses and 3 accelerations).

The next set of equations are the strain-displacement relations which relate the internal deformation of the body with its displacement field.

$$\epsilon_{ij} = \frac{1}{2}\left(\frac{\partial u_i}{\partial x_j} + \frac{\partial u_j}{\partial x_i} + \frac{\partial u_k}{\partial x_i}\frac{\partial u_k}{\partial x_j} \right) \quad \text{(summation in k)} \tag{7}$$

Where ε is the strain, u_i displacement in the x_i direction. For small strains the products of partial derivatives may be neglected.

The 6 strain-displacement equations introduce 3 unknowns and so 6 more equations are needed, those represent the mechanical constitutive model or response model and relate stresses with strains. There are 3 main fields that attempt do describe material behaviors, Elasticity, Plasticity and Rheology. For each field there are several models with varying degree of approximation suited for different materials and/or deformation regimes. The model of relevance for the cases studied in this thesis is the Linear Elasticity model which for an isotropic material states:

$$\sigma_{ij} = \frac{E}{1+\nu}\left[\epsilon_{ij} + \delta_{ij}\frac{\nu}{1-2\nu}\epsilon_{kk} \right] \quad \text{(summation in k)} \tag{8}$$

Where E is the Young's modulus, v the poison coefficient and δ the Kronecker delta.

Substitution on the first set of equations results in a system of 3 partial differential equations for the displacements, the boundary condition for the solid fluid interface is that the fluid stresses be equal to the solid stresses, when the solid is not free falling in the fluid boundary conditions for the displacements must also be applied.

2.2 Numerical Methods

This work's focus is not on numerical methods therefore only a brief introduction of the methods used by each code will be given. Coupling algorithms will be given more attention because understanding their characteristics and limitations is key in solving FSI problems.

2.2.1 – Brief review of available methods for FSI

The methods used in FSI fall in two broad categories, the monolithic category in which a single set of modified equations is solved in a single domain comprising the fluid and solid, the partitioned category in which each set of equations is solved in the corresponding domain.

In the partitioned approach a clear separation between solid and fluid exists, therefore three domains must be considered, the solid, the fluid and the mesh. In this approach both meshes must follow (conform to) the motion/deformation of the solid so the interface between the two domains can be maintained, because of this the methods of this category are also called conforming mesh methods. One of the most popular methods in this class is the Arbitrary Lagrangian Eulerian (ALE) technique of Souli and Benson [2010], albeit usually associated to FEM this is the method used by STAR-CCM+ (a FVM solver), in this method the flow equations are modified to account for mesh motion by adding grid flux terms (essentially the volume swept by the faces per unit time).

The main advantage of this class of methods is convenience, there is no need to develop a code from the root since existing verified codes can be used.

The main disadvantage is the need to solve equations to update the fluid mesh which adds to the computational effort. Contact problems can't be solved without overset meshes.

The main challenges are the interpolation of data, forces from the fluid side to solid side and displacements the other way around, across the interface in a consistent (same virtual work on the two meshes) and conservative manner (equal magnitude of forces) and dealing with tightly coupled systems.

The first challenge is due to the surface meshes of the interface not being equal since the fluid mesh is usually fine near solid boundaries and the solid mesh only needs to be fine near geometric details leading to stress concentration. In the point match method mesh nearby points (different measures of distance are used by different authors) are linked by rigid elements, this methods not always ensures both properties, in some methods a NURBS representation of the deformed surface is used to transfer displacements, neither property is enforced. A method that has both properties is the mortar method, an artificial structure is constructed around the solid with a mesh defined by the points of both surface meshes, fluid forces are applied to the points from the fluid mesh while the others are weld fixed, the reactions are then applied to the solid. Knowing the displacements on the points of the solid mesh the displacements of the fluid mesh points must be such that the artificial structure is in equilibrium.

To update the coordinates of the mesh points away from the interface several possibilities exist, in the mortar method one solves a elasticity problem for the fluid domain using the boundary displacements

as loads, STAR-CCM+ uses multiquadratic interpolation to generate an interpolation field from the displacements of the control points (boundary points usually). The solid mesh dispenses this step since the solid stress problem is solved in a Lagrangian frame of reference.
In the monolithic approach the mesh is the same for both domains and is stationary (non conforming), the flow equations are modified trough the addition of source terms to account for the presence of the solid. The most popular methods in this category are the Immersed Boundary Method and the Immersed Volume Method.
Methods in this class are robust because the mathematic formulation of the problem facilitates an implicit solution of the system of equations. They save on computations by not requiring mesh update. For the same reason solution of contact problems is straightforward.
The main cons are: the need to develop the whole code; fine meshes are needed to sharply capture a solid boundary, this coupled to large solid displacements may lead to meshes with large cell counts, this can be overcome with mesh adaptation strategies.

2.2.2 – STAR-CCM+/ABAQUS Numerical Methods

The purpose of the finite volume method (FVM) is to transform a set of partial differential equations into a system of algebraic equations, to do this the equations are integrated over a control volume (a cell in FVM nomenclature) and by application of Gauss's divergence theorem and considering some quantities to be constant over the cell faces the integral is transformed into a summation of fluxes entering the control volume, this makes the method local and globally conservative. Subdividing the computational domain in several cells, i.e. creating a mesh, results in a system of algebraic equations.
Meshes can be divided in two broad categories, structured and unstructured, in structured meshes simply knowing the index of a cell is enough to know its neighbors, in unstructured meshes the connectivity information needs to be stored. Most commercial codes use unstructured meshes because its easier to generate them for complex geometries.
For the fluid-flow equations the fluxes appear from the convective and diffusive terms. The discretized form of the convective term is a mass flow rate, since in most FVM codes the unknowns are placed in the cell's centroid it is necessary to use numerical schemes to relate face values with cell values. In STAR-CCM+ case the scheme used is either the first or the second order upwind scheme, the transition is made trough the use of a limiter (for laminar flow the limiter used is usually the Venkatakrishnan limiter), limiters don't allow new extrema to be formed and this avoids non realistic solutions to be calculated. The discretized form of the diffusive term is a finite difference equation for a gradient.
Because unstructured meshes don't usually have regular shapes this non orthogonality needs to be corrected for the method to remain second order, this correction uses the cell centered gradient and is usually put as a source term to avoid destabilizing the iterative solution of the system of equations. For this reason highly skewed cells are to be avoided because they'll make convergence slower.
The unsteady term is discretized by the finite difference method, STAR-CCM+ uses implicit second

order differences by default.

Because there's no transport equation for pressure when solving the fluid-flow equations some form of pressure-velocity coupling must be used, in pressure based solvers this is usually done using SIMPLE (Semi Implicit Method for Pressure Linked Equations). Simple is a predictor-corrector method, starting from guessed velocity and pressure fields the momentum equations are solved, with the velocities obtained the pressure correction equation is solved and the guessed pressure field is updated, the velocities ate updated with the velocity correction equations and the process is repeated until sufficient level of convergence is attained (i.e. the corrections fall to a low value).

In the finite element method (FEM) the computational domain is also subdivided, the subdivisions are called elements. FEM differs from FVM in that it considers that the unknowns vary according to some basis function inside each element, in FEM the unknowns are placed at the vertexes (nodes) of the elements.

The meshes can also be structured or unstructured but the method doesn't need to change to accommodate this.

The end result as in FVM is to obtain a system of algebraic equations, a coefficient matrix is assembled based in the connectivity information (which element nodes share a mesh node) and in the coefficients of the basis functions. In structural mechanics this matrix is called the stiffness matrix and the unknowns are the displacements.

The time integration method used by ABAQUS is the Hilber-Hughes-Taylor, this method is second order implicit, allows fine tuning of the numerical damping and is unconditionally stable for linear systems.

2.2.3 – STAR-CCM+/ABAQUS Coupling Algorithms

Since the method used by STAR-CCM+ and ABAQUS if of the partitioned category special attention will be given to the coupling schemes available to them.

The role of coupling can be understood by picturing two time dependent systems in which the rate of change of a quantity depends on the present states of both systems, mathematically:

$$\begin{aligned} \dot{x_1} &= f_1(x_1, x_2) \\ \dot{x_2} &= f_2(x_2, x_1) \end{aligned} \tag{9}$$

When discretizing the above equations and trying to advance the solution in time three possibilities exist.

In explicit coupling quantities at time level n+1 are calculated based only on what its known at time level n, this is refered by ABAQUS as Jacobi coupling (for its resemblance with the linear equation solution method). This method allows the codes to run in parallel which is desirable from the computational point of view, however, the time step stability limit may be very small and the method is only first order accurate in time.

A more robust alternative is to stagger the solution of the system i.e. first one solves for x_1 and then

for x_2 using the value of x_1 at time level n+1. In ABAQUS nomenclature this is called Gauss-Seidel coupling also because of similarity with the linear solver. Although the stability limit increases this is also first order accurate and the codes can no longer run in parallel.

To achieve second order in time using explicit methods one needs to extrapolate values from past time levels, this will further reduce the stability limits making explicit coupling inadequate in many FSI cases.

The third alternative is implicit coupling, in its simplest form in the example of Gauss-Seidel coupling the value for x_2 would be used to re-calculate x_1 and this process would be repeated until satisfaction of some convergence criterion. This coupling scheme is stabler and second order accurate, it also allows under-relaxation in the inner iterations contributing to its stability. In the STAR-CCM+ / ABAQUS case the codes are run sequentially but it would be possible for them to run in parallel in a Jacobi manner, greater under-relaxation would possibly be required.

The downside of not executing the codes in parallel is that in cases where the fluid solver requires much more computational power (for example when performing Large Eddy Simulation) it is not practical to halt its execution while the finite element problem is being solved, because most times the solid stress code will not be able to take advantage of the same number of processors. Methods designed for LES have this in consideration.

Advanced codes have a linearization step, when solving an inner iteration of the fluid problem this gives a solution influenced by what is expected to happen to the solid displacement, this increases the rate of convergence and the robustness of the code.

3. Two Dimensional Plate Free-Fall Under Cross-Flow

It was Maxwell who first presented a qualitative description of the motion of free-falling strips of paper in the 19th century [Maxwell, 1854], before aerodynamic theory had been developed. Recent studies employing numerical simulation or experimental techniques such as high speed image acquisition provided knowledge on average quantities like descent angle, vertical, horizontal and angular velocities and the period of the motion [Dupleich, 1941; Hirata, 2009].

Identified different motion regimes (tumbling, fluttering, chaotic motion and simple perpendicular fall), how they are related with the body's geometry and fluid/material properties and how these parameters control the transition between regimes [Zhong, et al. 2010; Field et al. 1997; Belmonte et al. 1997].

Characterized instantaneous quantities proposing models for them [Pesavento et al. 2004; Andersen et al. 2005; Varshney et al. 2013; Kaneko et al., 1994].

Studies of plates in cross-flow have been conducted in the context of debris dispersion [Kalimpa et al. 2012] but not for a range of cross-flow velocities. The results of Kalimpa however showed that tumbling and fluttering motions do exist in the presence of cross-flow.

Two key parameters govern the motion regime of a free-falling disk, Reynolds number (Re, calculated with the average fall velocity) and dimensionless moment of inertia (I*, ratio between the disk's moment of inertia and an arbitrary measure of the moment of inertia of the surrounding fluid). For different values of this parameters the disk may tumble, flutter, fall perpendicular to its axis, follow a spiral pattern (this motion can be coupled with fluttering) or have a chaotic behavior (usually tumbling in alternate directions) [Zhong et al. 2011], see figure 3.1.

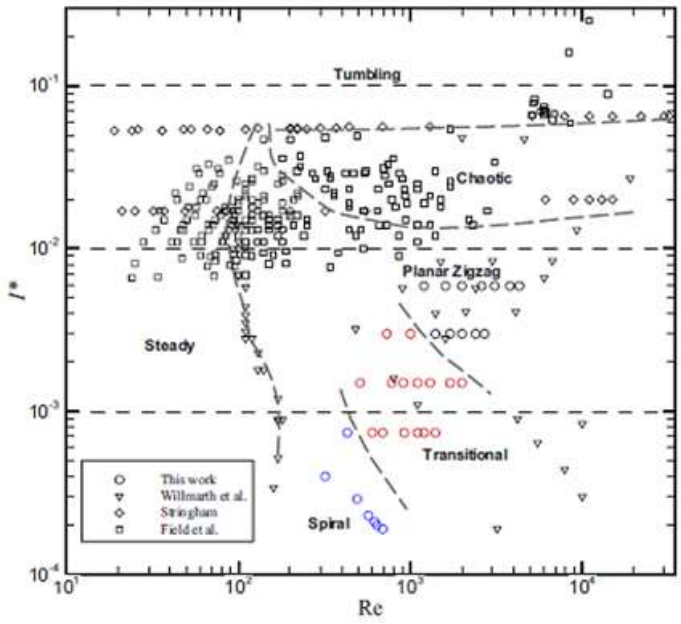

Figure 3.1 – Re-I* Diagram for disks [Zhong et al. 2011].

A free-falling plate can only exhibit 4 motion regimes, tumbling (associated with large I*, see figure 3.2 a), perpendicular fall (associated with low Re and moderate I*), fluttering (for low I* and moderate-high Re, see figure 3.2b) and chaotic motion (moderate I* and moderate-high Re).

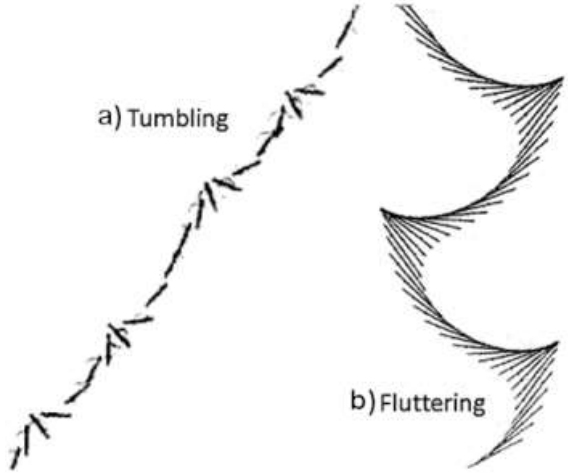

Figure 3.2 – Tumbling and Fluttering of a 2-D Plate [Belmonte et al. 1998].

A sphere falling in Stokes flow will reach a terminal velocity such that the drag force balances its buoyancy corrected weight. If cross-flow is added to the situation above a force in the horizontal direction will develop proportional to the difference between cross-flow and sphere horizontal velocity, this will make the sphere accelerate until the horizontal force vanishes, at this point in time the sphere's horizontal velocity will match the cross-flow velocity and the fall velocity will still be the same.
The conclusion of this thought experiment is obvious, Stokes flow is governed by linear equations. What's not obvious is what happens at higher velocities when advection effects are significant, and the motion regimes more complex.
For a fixed Re and varying I* the chaotic regime lies between the tumbling and fluttering regimes, in this work we investigate what influence can cross-flow have on tumbling and fluttering (for instance, can a periodic motion become chaotic due to its presence? Or can it force a transition between regimes?).

3.1 Numerical Procedure

The equations were solved in a sliding domain, composed of a circle able to rotate with the plate and a large non-rotating rectangle (see figure 3.3a), the unstructured finite volume commercial code STAR-CCM+ v8.02 was used. At high cross-flow velocities (above 2m/s) convergence problems caused by flow reversal at the pressure boundary made it necessary to use overset mesh, for that a stationary rectangular domain was added (figure 3.3b), in this region a cartesian mesh was used (whereas the other regions were meshed with polyhedral cells).
Pressure and velocity boundary conditions were used, the pressure boundary is either on the left or right side depending if the plate is moving to the right or to the left respectively. On the remaining 3

sides the 3 velocity components are specified.

The dimensions of the domain were indexed to the dimensions of the plate, refinement zones were included near the plate including a prism layer on the surface. Prism layers were used on both sides of the circular interface to reduce interpolation errors across it, also with the same objective the time step was limited to maintain vertex displacement below face length.

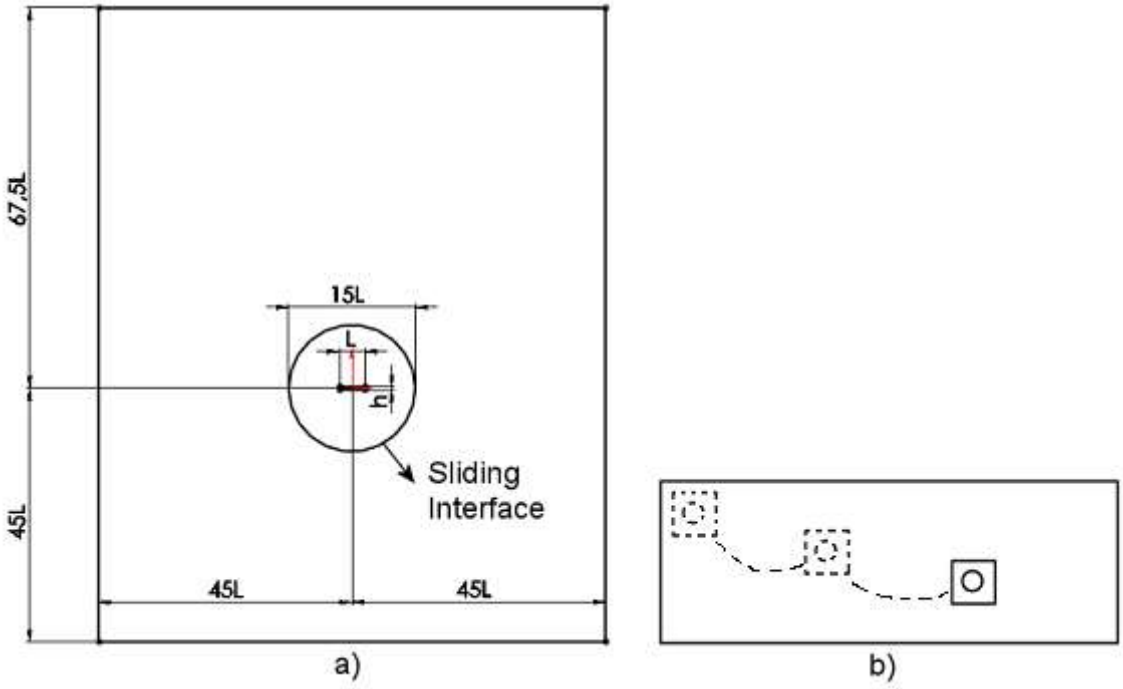

Figure 3.3 – a) Sliding domain; b) Overset domain (dimensions not to scale).

For a validation study and more details about the mesh used (for instance size of the refinement zones) the reader should consult the work by Zorzi [2013] where the numerical model here described is compared with the experimental results of Andersen et al. [2005] and numerical results of Jin and Xu [2008]. For simplicity only the results obtained by him with a mesh of 60k cells are reproduce here (table 3.1), for the properties of the plate and fluid see section 3.2.1.

In the present work the domain used was wider than the one used by Zorzi because it was speculated that the cross-flow could carry the wake farther away from the plate, the total number of cells is 90k, the results for the no cross-flow case are also presented in table 3.1.

Table 3.1 – Comparison of numerical and experimental results.

	Mean horizontal velocity [cm/s]	Mean vertical velocity [cm/s]	Mean angular velocity [rad/s]
Experimental [Andersen]	15,9	-11,5	14,5
Numerical [Jin and Xu]	15,1	-11,8	15,0
Numerical [Zorzi]	15,6	-11,0	15,3
Present Work	15,5	-10,4	14,7

3.2 Results

To analyze the effect of cross-flow we looked into average velocities and how they correlate with each other. Due to large cycle to cycle variations (see the u-v attractor of figure 3.6 for the no cross-flow case) instantaneous quantities were not analyzed, instead we resorted to phase averaging to obtain a representation of the forces and velocities during an average period. We start this section by introducing the quantities of interest used to analyze the effects of cross-flow.

Mean velocity during a period, for the tumbling motion observed in this work a period is 180º of plate rotation (under some circumstances a period can have 360º), the mean velocity during this time is the variation of displacement (or rotation) over the time needed to perform the half rotation. For fluttering the angular position at the beginning and end of a period is the same as well as the direction of travel (left to right or vice versa).

The mean velocity for the trajectory was calculated fitting a linear polynomial to the displacement(rotation) vs time curve, an integer number of motion periods was used.

As mentioned earlier, with the dimensions and properties chosen the tumbling case exhibited large cycle to cycle variations in the velocities and forces (its worth noticing that experimental results [Andersen et al. 2005] also show this variations), a physical explanation for them is the following: because of the low moment of inertia of the plate, at the point where the plate goes trough the vertical position and the angular velocity is lowest the wake has a significant influence on the start of the new period. If the vortex shedding is not a multiple of the tumbling frequency its very easy for the conditions at the beginning of the new period to be completely different resulting in different forces and velocities during the period, this can be seen in images 1 and 6 of figure 3.7.

Due to these cycle to cycle variations its not possible to compare instantaneous values for various cross-flow velocities. We resorted to phase averaging to obtain a representation of a mean motion period. For tumbling, because the angular position vs time curve is injective the averages were made at fixed angular position intervals. In fluttering angular position is a periodic function therefore the periods were first separated and the averages were then performed at fixed normalized time (time divided by the duration of a specific period) intervals.

Average values of velocity and pressure fields were not calculated, there are more cycle to cycle variations in this quantities than in forces and velocities (which result from integration) and so a very large number of samples would be required.

When presenting the mean velocities during a trajectory the 95% (±2σ) confidence bounds are also represented, because the mean velocity during the trajectory is the mean for a large number of cycles, from the central limit theorem the trajectory mean will be normally distributed and the standard deviation can be calculated knowing the number of cycles and the standard deviation of the mean velocity during individual periods.

$$\sigma_{\text{trajectory}} = \frac{\sigma_{\text{period}}}{\sqrt{N_{\text{periods}}}} \tag{10}$$

In the figures displacement is made dimensionless by plate length (L) and velocities by theoretical

terminal velocity [Andersen et al. 2005].

$$v_i^* = \frac{v_i}{V} \qquad V = \sqrt{2\left(\frac{\rho_s}{\rho_f} - 1\right) h\, g} \tag{11}$$

Where g is the acceleration of gravity and the subscripts “s” and “f” denote solid and fluid respectively. Angular velocity is made dimensionless dividing tip velocity due to rotation by the terminal velocity.

$$\omega^* = \frac{\omega\, L}{2\, V} \tag{12}$$

Time is made dimensionless dividing it by the time needed to travel one plate length at terminal velocity.

$$t^* = t\frac{V}{L} \tag{13}$$

Forces by the buoyancy corrected weight $((\rho_s - \rho_f) hLg)$ and moment by this value multiplied by plate length.

3.2.1 Tumbling

The tumbling study was conducted for an aluminum $(\rho = 2700 kg/m^3)$ plate of thickness 0.81mm and aspect ratio 8 falling in water $(\rho = 1000 \mathrm{kg}/m^3,\ \nu = 8.8871 \times 10^{-7} m^2/s)$.

Figure 3.4 shows x-y trajectories for various cross-flow velocities, for clarity the number of cycles shown is limited.

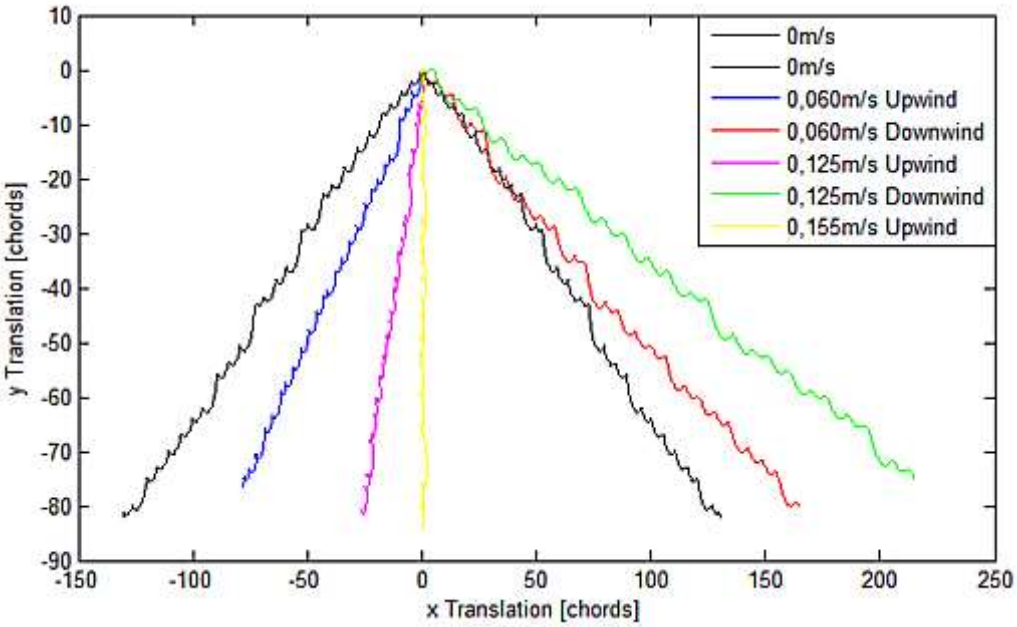

Figure 3.4 – Trajectories in the x-y plane for different values of cross-flow.

To compare trajectories at higher cross-flow velocities its useful to consider an observer moving at the cross-flow velocity, see figure 3.5. When looked at by a moving observer all trajectories are similar to

the ones without cross-flow, the distances covered in one period and the whole trajectory are similar, the apparent descent angle, etc. The differences in the trajectories are in part due to the cycle to cycle variations described in section 3.2.

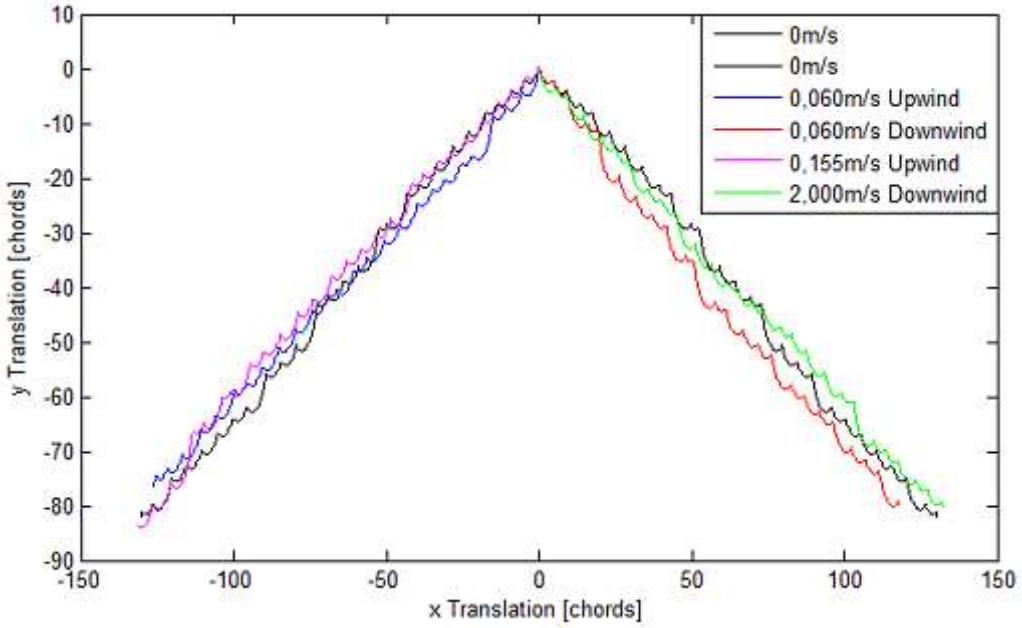

Figure 3.5 – Trajectories as viewed by an observer moving at the cross-flow velocity.

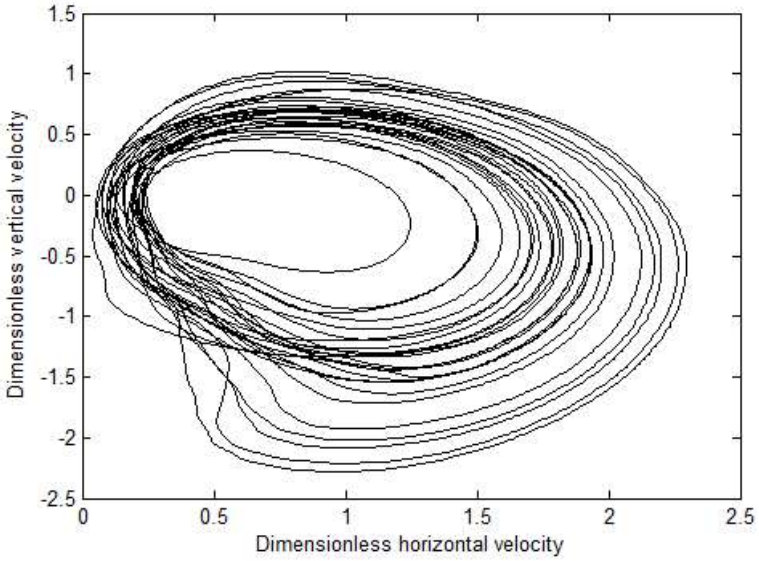

Figure 3.6 – Attractor of the no cross-flow case projected in the u-v plane.

Figures 3.7 and 3.8 show vorticity contour plots at various instants of a tumbling cycle at two cross-flow velocities, 0 and 0.155m/s (vertical descent) respectively. As mentioned in section 3.2 it's when the plate is vertical that there's a possibility to reverse the direction of tumbling, as can be seen in the figures there's no significant change in the wake or in the position of the plate relative to it during this critical periods.

With this hypothesis in mind, that the cross-flow, on average, only changes the horizontal translation velocity the forces and velocities were studied.

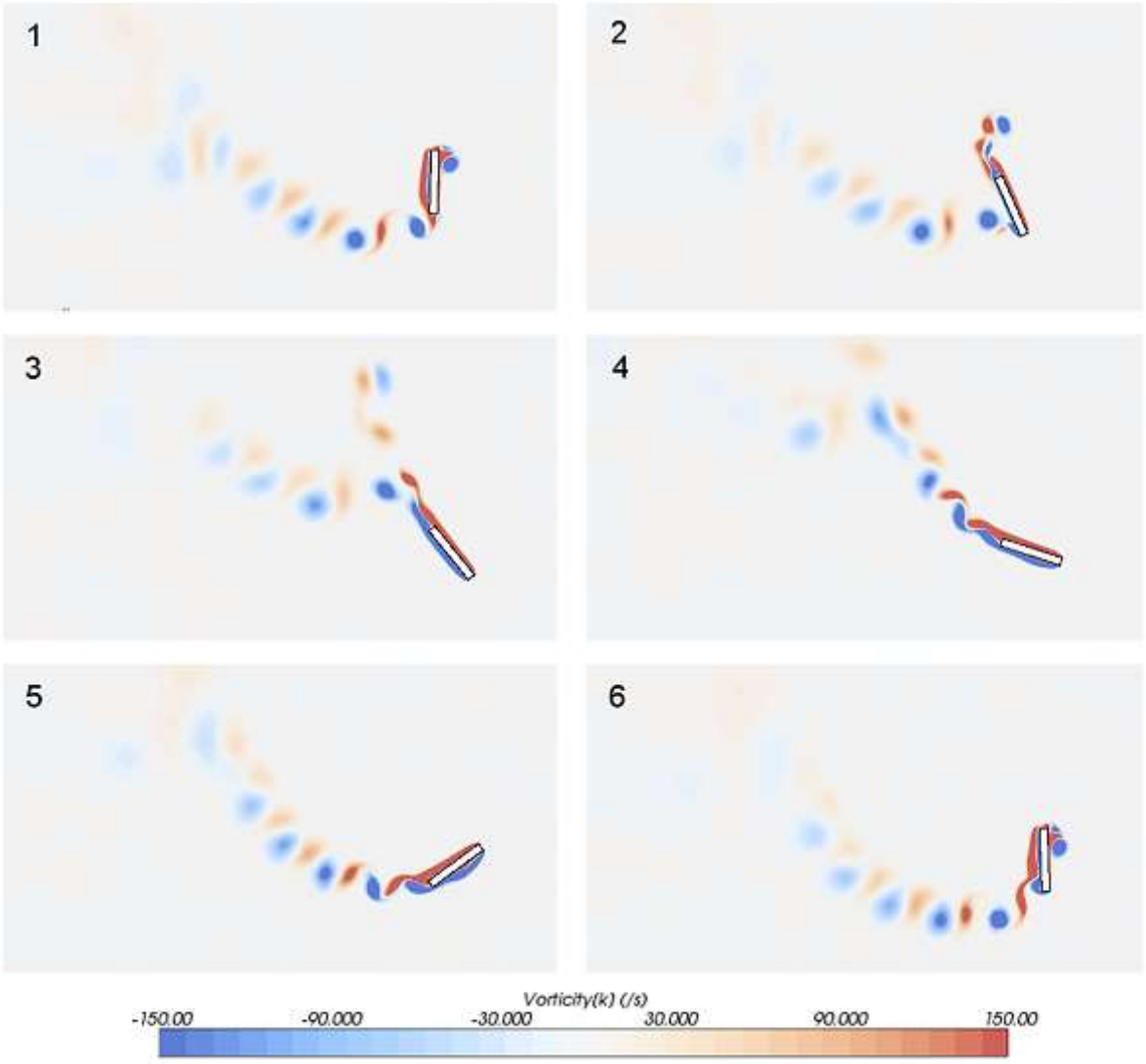

Figure 3.7 - Vorticity with no cross-flow.

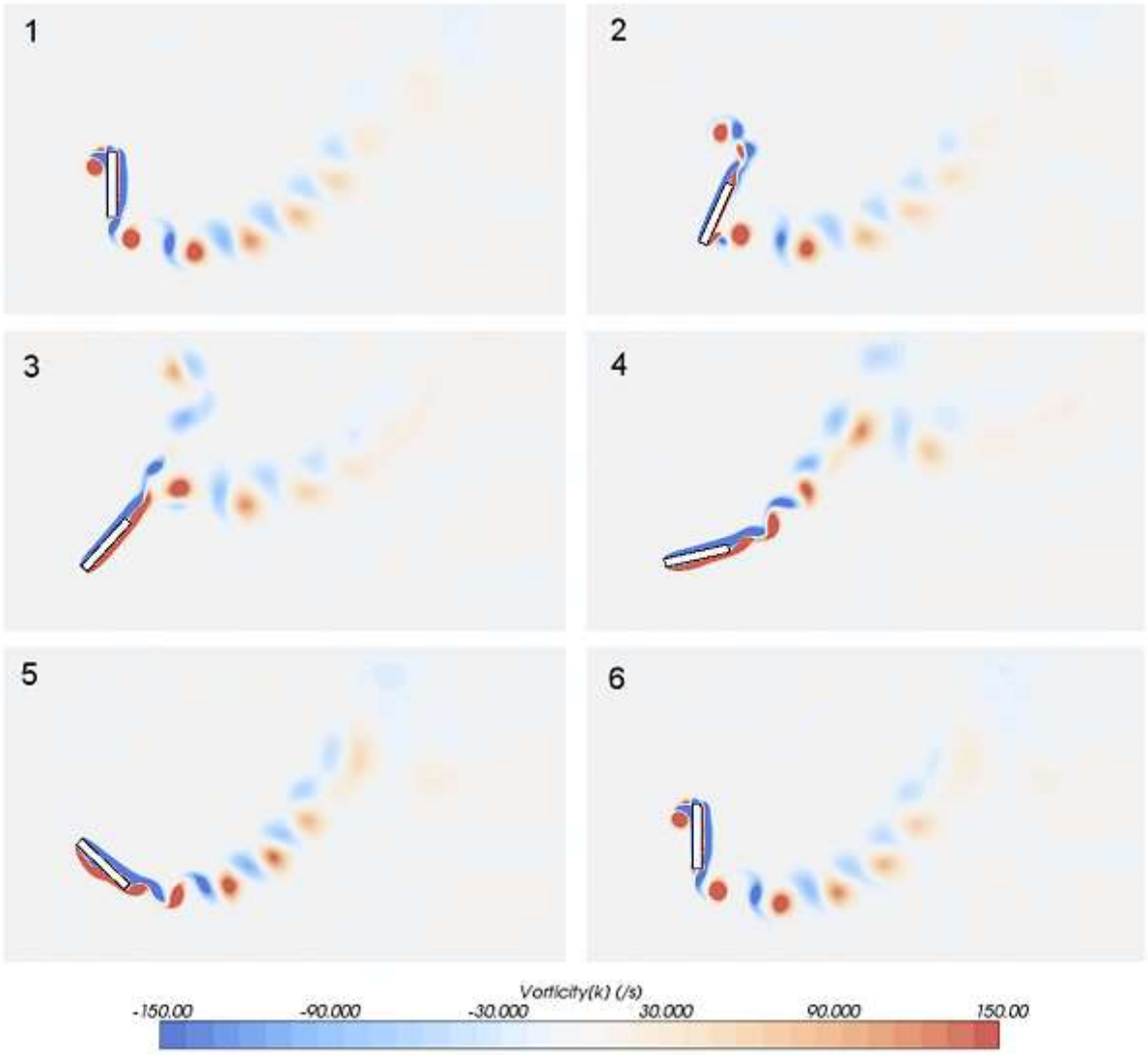

Figure 3.8 - Vorticity with cross-flow velocity of 0,155m/s.

Figure 3.9 shows the absolute difference between average horizontal velocity and cross-flow velocity vs the cross-flow velocity. This difference is almost constant and equal to the value for no cross-flow (0.9432).

Figure 3.10 shows the average vertical velocity vs the cross-flow velocity. Again we observe that the values show no consistent variation to indicate that the cross-flow may alter the fall velocity of the plate. Figure 3.11 shows the results for angular velocity.

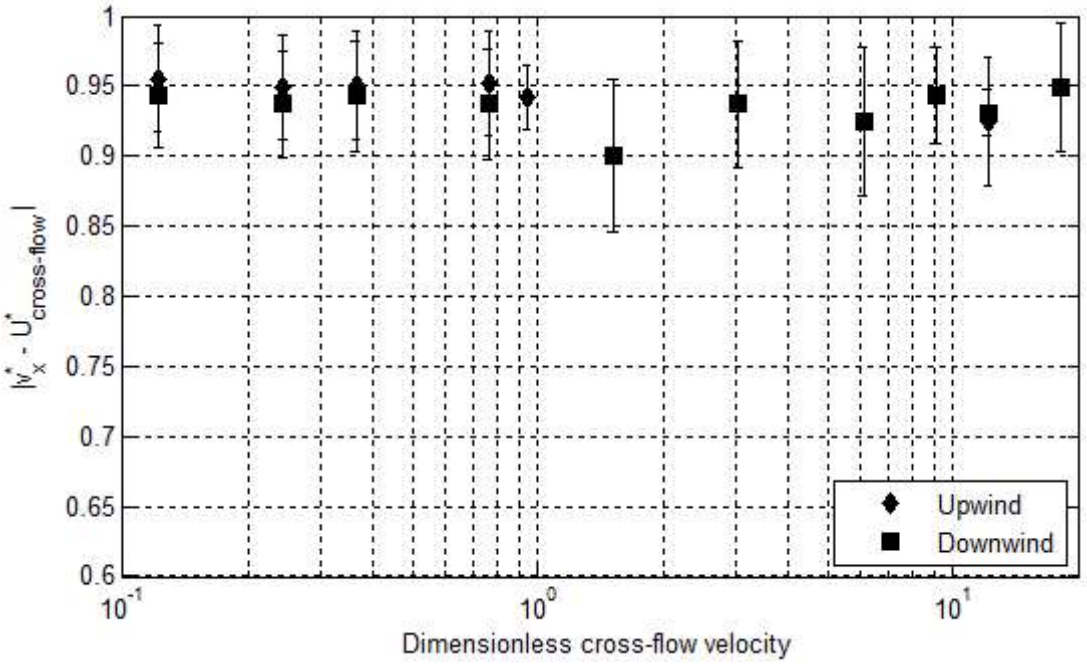

Figure 3.9 – Absolute difference between mean horizontal velocity and cross-flow velocity.

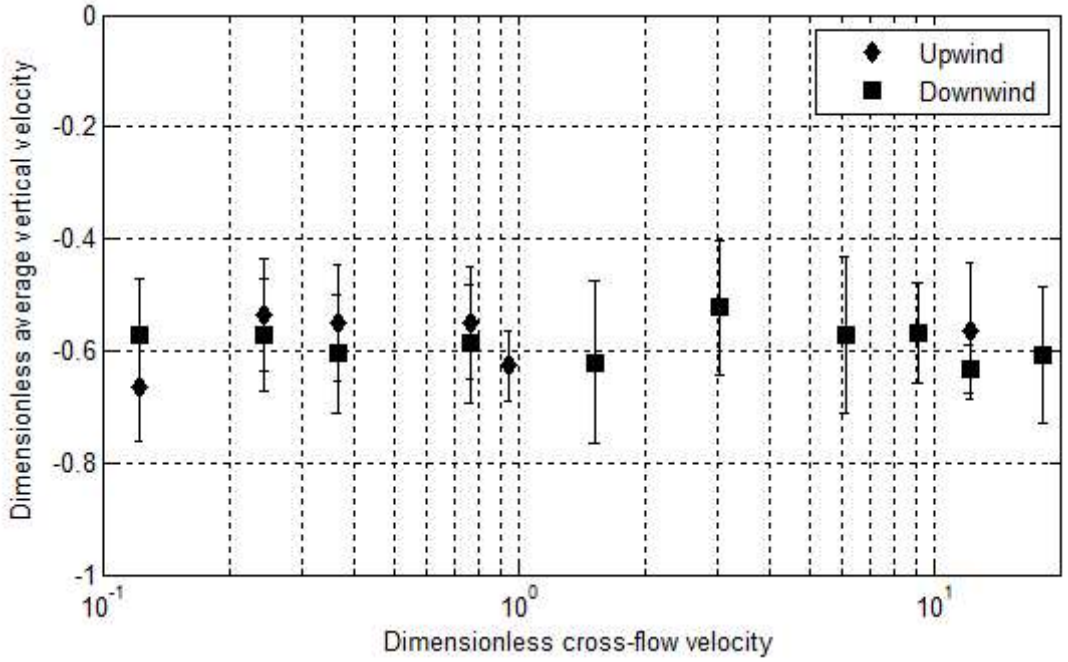

Figure 3.10 – Average vertical velocity vs cross-flow velocity.

All this data suggests that cross-flow has no effect on the average velocities, it merely adds to the horizontal velocity. Also the plate is able to tumble “against” cross-flow velocities 20 times greater than the mean fall velocity.

With the data of the two longest simulations, tumbling against a 0.155m/s cross-flow (66 cycles, vertical descent) and in favor of a 2m/s cross-flow (140 cycles), an hypothesis test was performed for

the vertical and angular velocities and for the absolute horizontal velocity relative to the flow, at a significance level of 5% the hypothesis that the two cases share the same population mean cannot be discarded for any velocity.

Further evidence for this hypothesis is provided by the phase averaged forces and moment plots, see figures 3.12 to 3.14. The plate's initial position is -45º from horizontal.

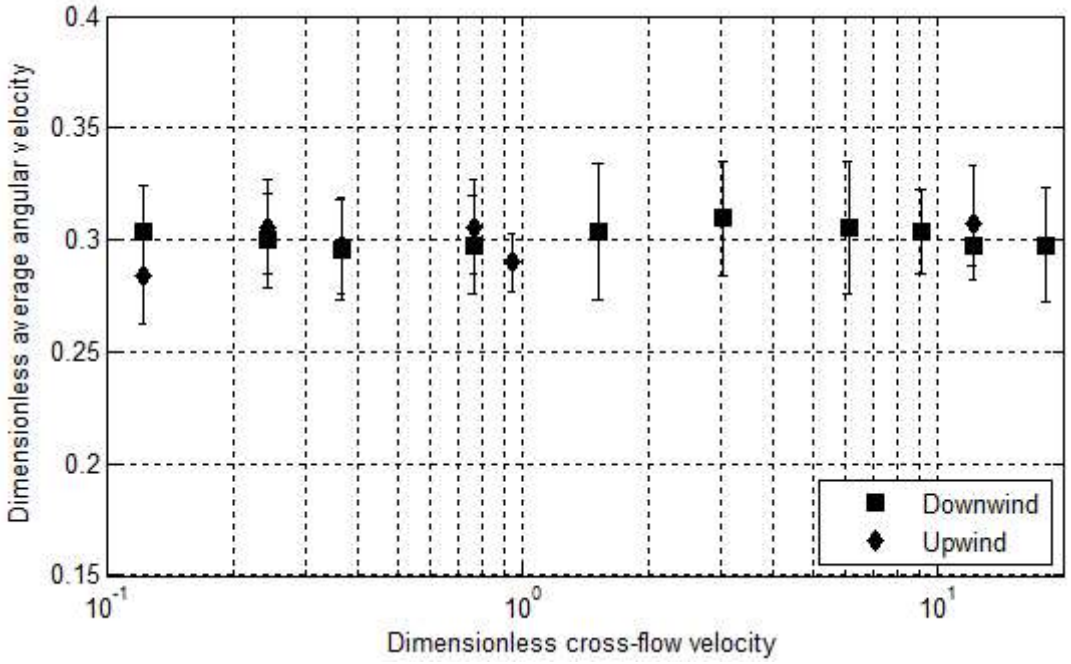

Figure 3.11 – Average angular velocity vs cross-flow velocity.

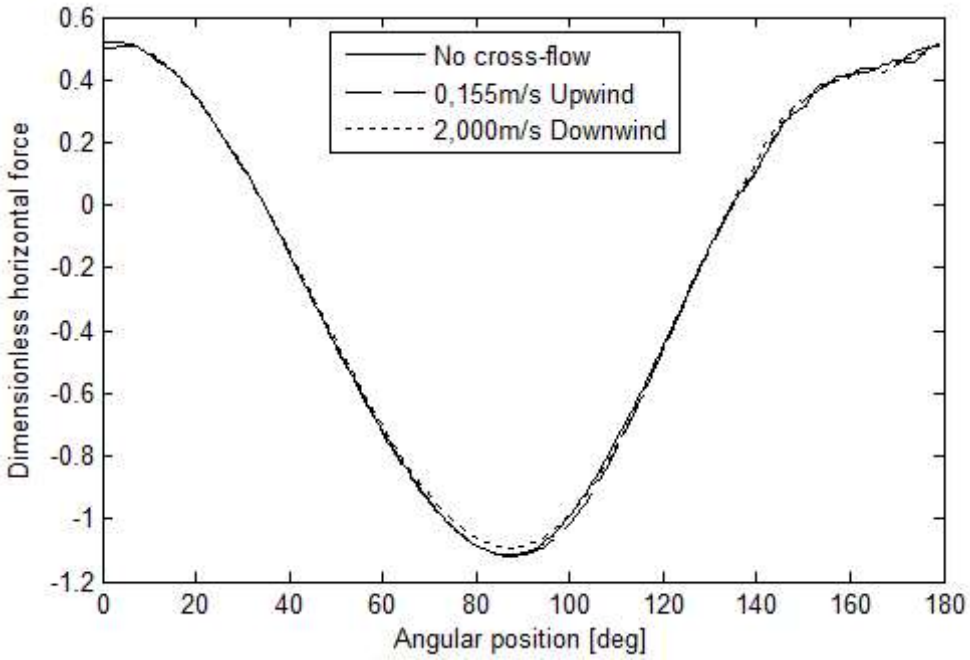

Figure 3.12 – Dimensionless horizontal phase averaged force.

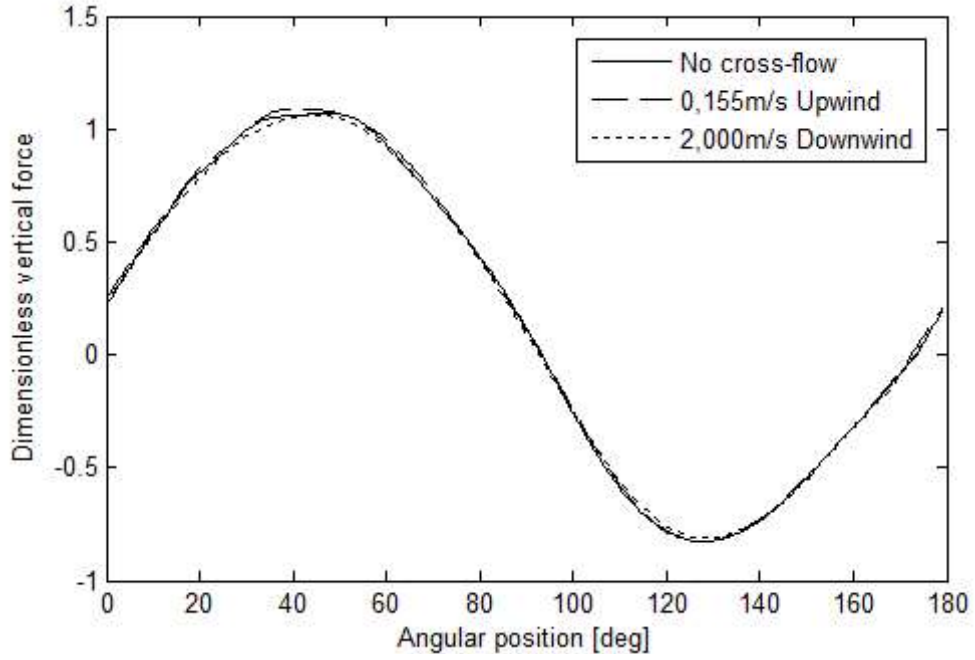

Figure 3.13 – Dimensionless vertical phase averaged force.

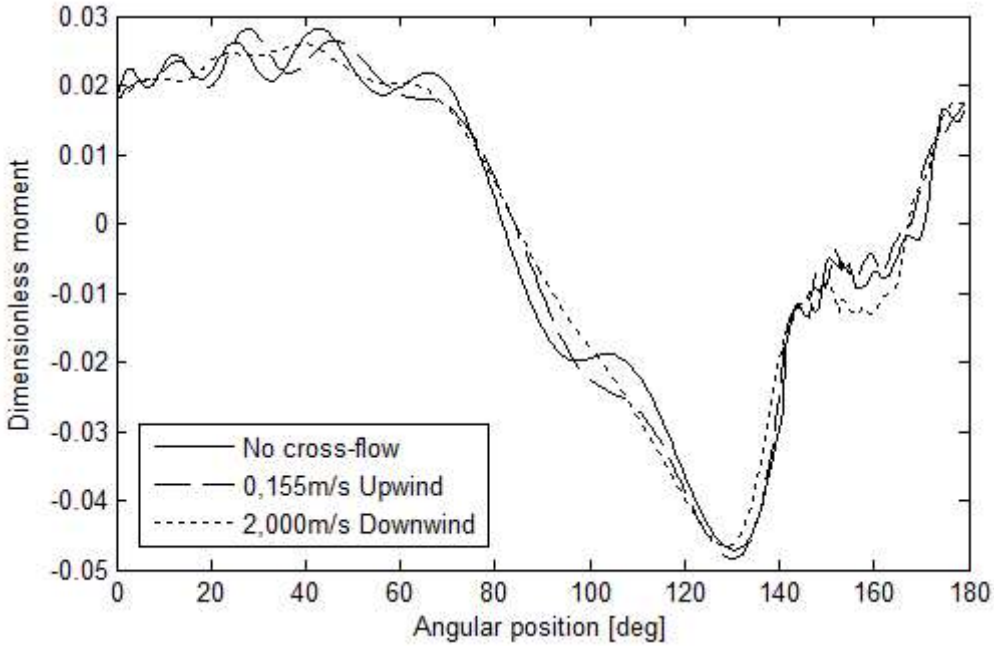

Figure 3.14 – Dimensionless phase averaged moment.

The forces are almost identical, the moment has bigger differences because there's not enough samples to filter the influence of vortex shedding, note that the 2m/s line, obtained with a greater number of cycles (140 vs 66 from the vertical trajectory), is smoother.

It could be possible that the presence of cross-flow had no effect on the average velocities but could change the short term behavior, we exclude this by analyzing the correlation between the mean

vertical and angular velocities during a tumbling cycle, see figure 3.15. It's known that most of the lift comes from the plate's rotation [Pesavento et al. 2004] therefore the greater the angular velocity the slower the descent, what is interesting to note is that the relation between the two velocities follows the same trend irrespective of the cross-flow velocity.

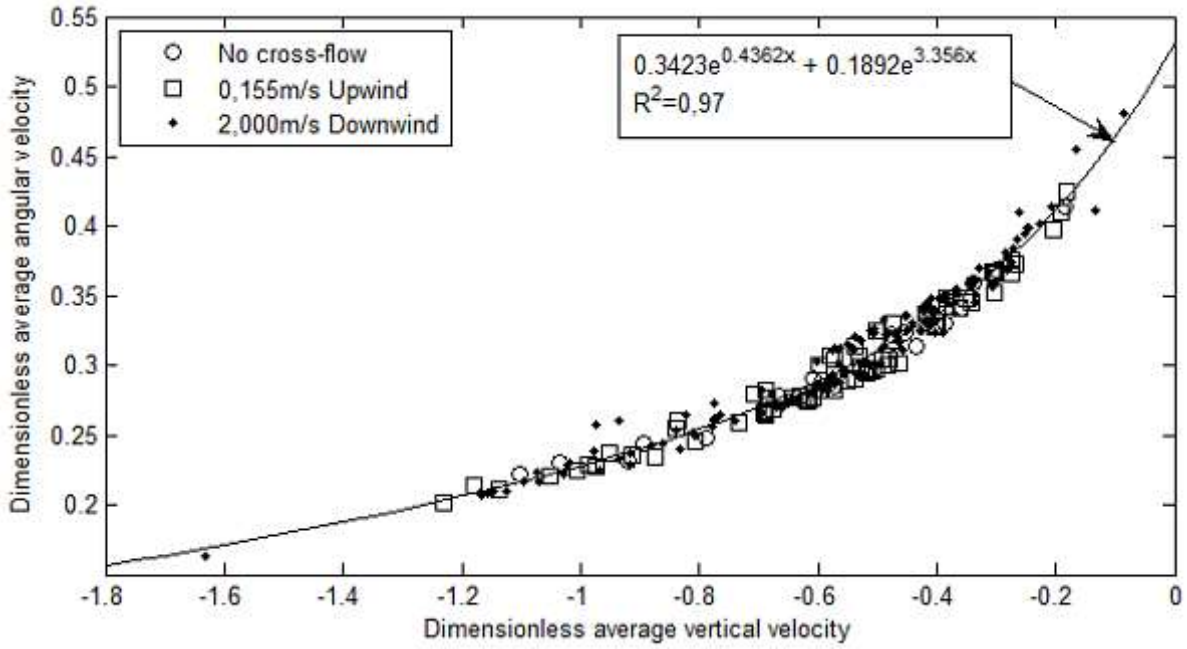

Figure 3.15 – Angular vs fall velocity, mean values during a cycle.

3.2.2 Fluttering

For the fluttering study the aspect ratio was changed to 14, all other variables were maintained.
Because the fluttering motion resulting from the parameters chosen showed little cycle to cycle variations (as can be seen from the x-y trajectories in figure 3.16) only 5 periods were used for the averages. Fluttering is inherently less prone to cycle to cycle variations because of the larger moment of inertia of the plate and because the plate doesn't go trough the vertical position, therefore when it initiates the descent, upon reaching maximum inclination, the pitching moment developed will counter the rotation of the plate. Figure 3.17 shows vorticity contour plots for fluttering without cross-flow, because of symmetry only half period is represented.

Figures 3.18 trough 3.21 show relative horizontal and vertical velocity, angular position and velocity, respectively, as a function of dimensionless time. In the plots the initial position of the plate is horizontal (0º).

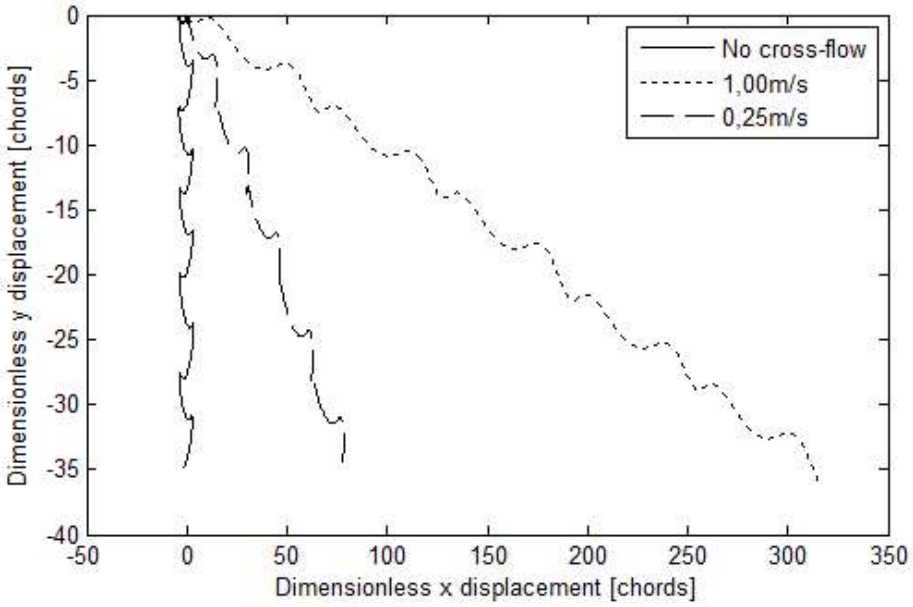

Figure 3.16 – Fluttering trajectories in the x-y plane.

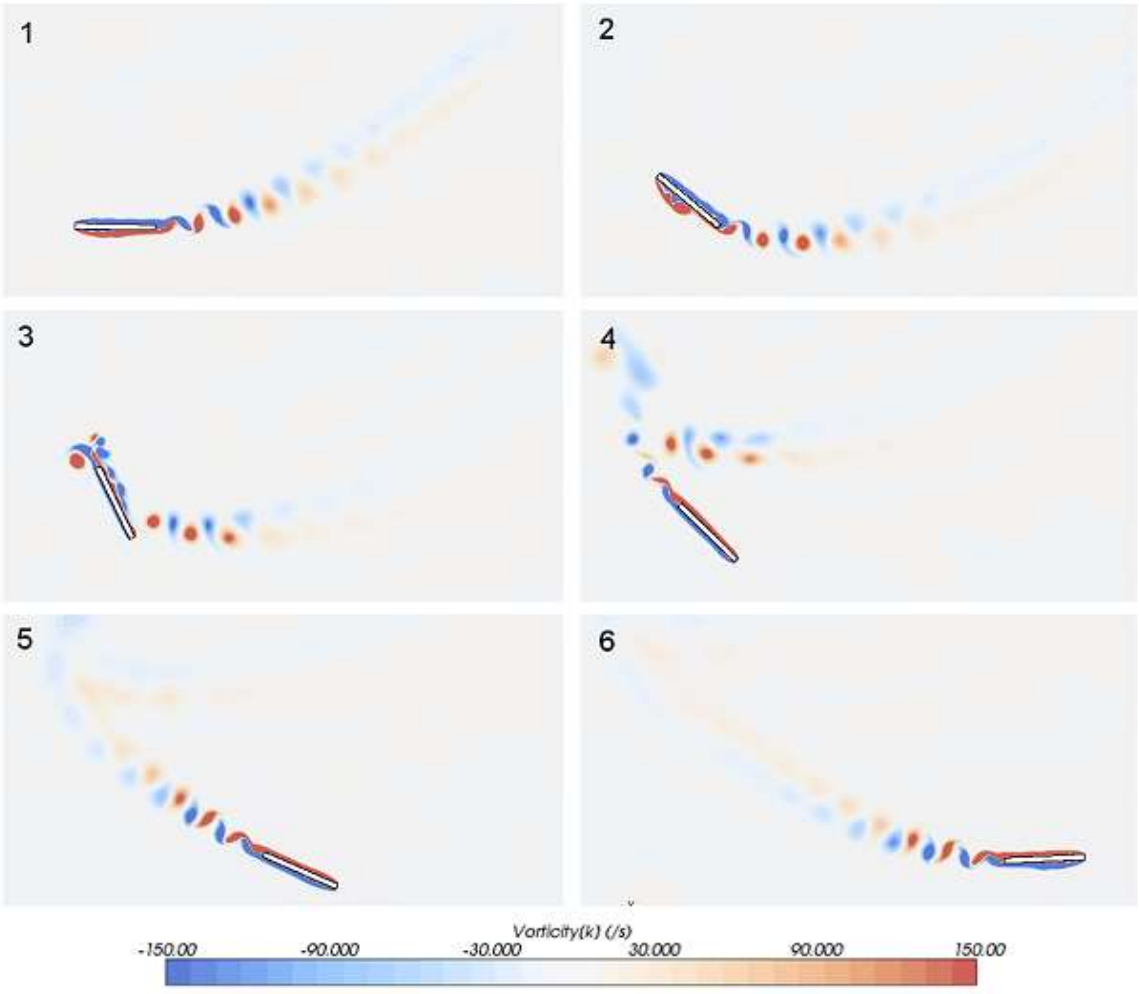

Figure 3.17 – Vorticity contour plots for fluttering without cross-flow, half period represented.

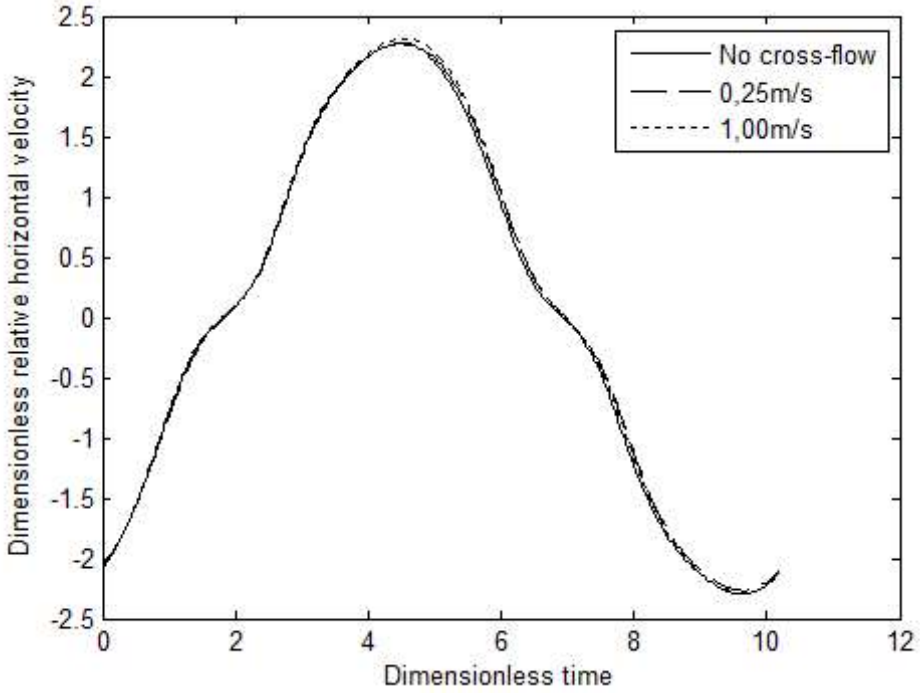

Figure 3.18 – Relative horizontal velocity at different cross-flow velocities.

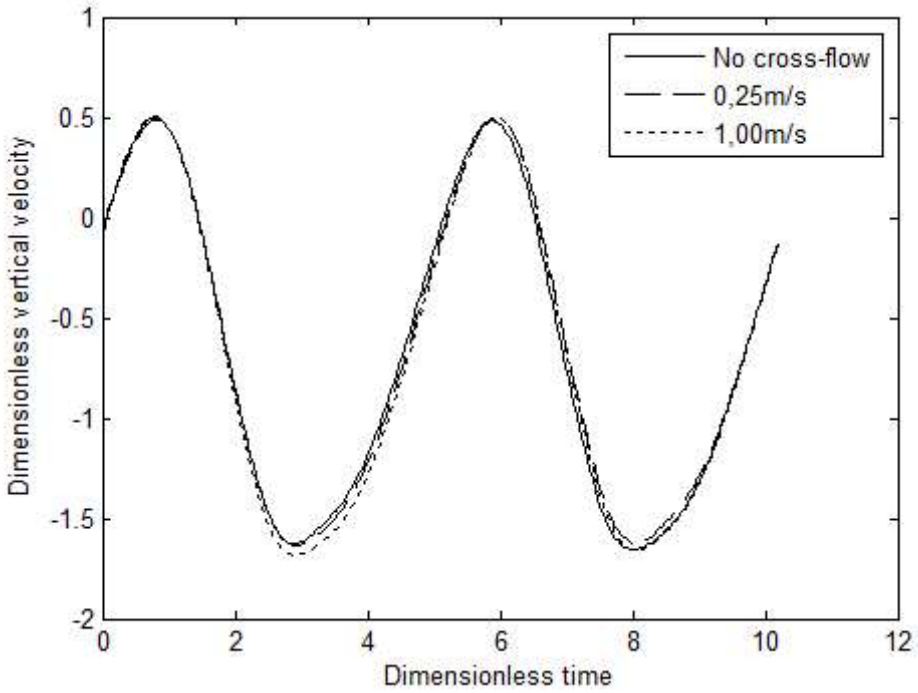

Figure 3.19 – Vertical velocity at different cross-flow velocities.

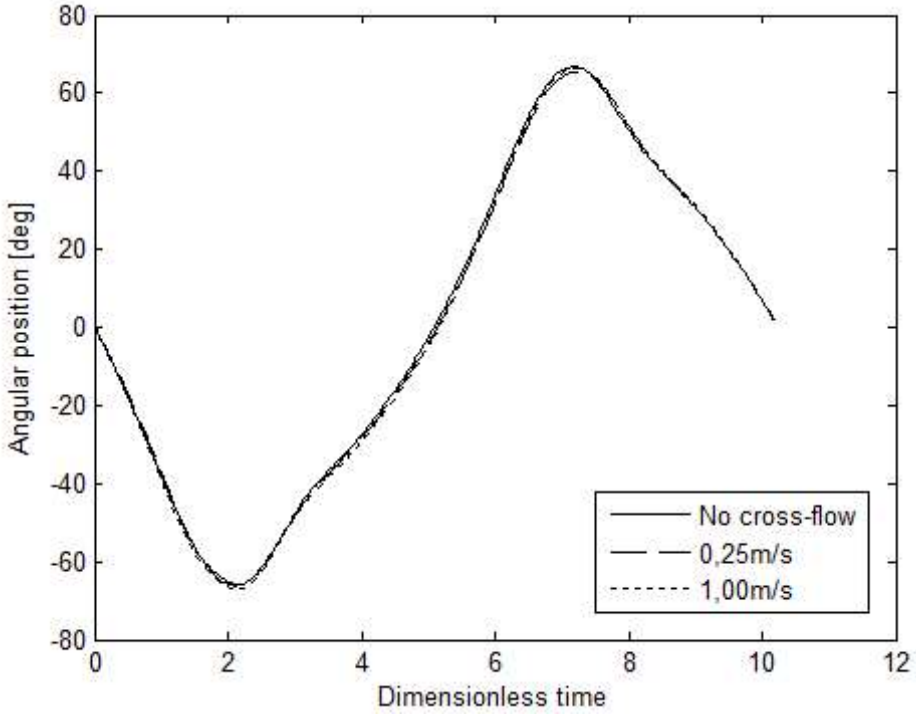

Figure 3.20 – Angular position at different cross-flow velocities.

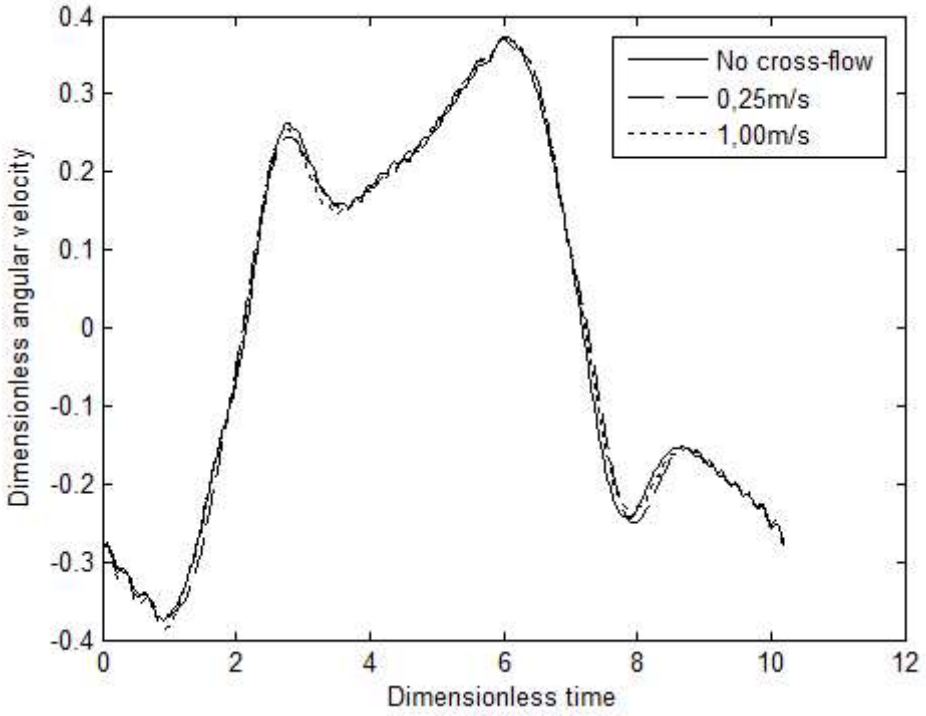

Figure 3.21 – Angular velocity at different cross-flow velocities.

For fluttering we observe the same behavior of tumbling, the motion regime does not change nor the velocities during a period, the cross-flow velocity adds to the horizontal velocity.

3.3 Analysis

In the two cases studied in this work the presence of cross-flow had no effect on the motion regime, the only quantity changed by it was the translation velocity in a linear fashion. It is very interesting to observe such linear behavior in physics governed by non-linear equations. We note that the velocity field does not change linearly like the plate's velocity, if it did the necessary pressure field to sustain it (i.e. respect conservation of momentum) would produce an additional downward force of magnitude $\rho h L \omega U_{CF}$ (h is plate thickness, L length, ω angular velocity and U_{CF} the cross-flow velocity, see annex A for the demonstration).

A possible explanation for the behavior of the plate is the following: If the velocity field is perturbed, increasing slightly the u component, the overall lift would decrease. This in turn would make the plate fall faster (decreasing the plate's v velocity component), but this increases the angle of attack during the whole cycle thus restoring lift (see figure 3.22 where a fluttering period is used as example, for tumbling the results are the same, see figure 3.23 for the axis convention). This is a suitable explanation only for what happens with very small perturbations, as was already demonstrated the changes in the velocity field cannot be so simple.

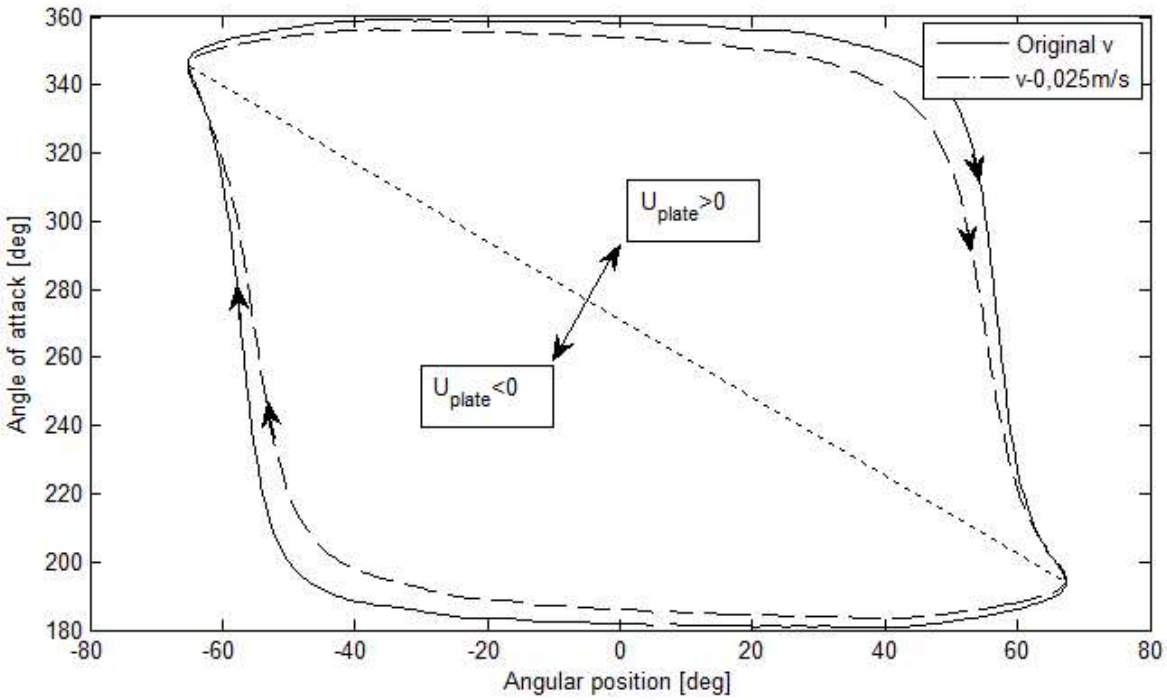

Figure 3.22 – Effect of increasing the descent rate on the angle of attack during a fluttering cycle.

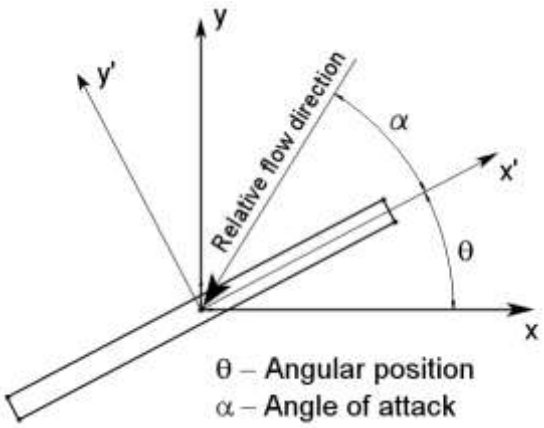

Figure 3.23 – Conventions for measuring angular position and angle of attack.

4. Study of Elastic Coupling Case

This chapter is dedicated to the FSI field of elastic-coupling. Problems in this field are characterized by the interaction of a deformable but not movable (some boundary will be fixed) structure with a fluid. In the recent years a number of verification and validation cases have been developed, to name a few: the benchmarks by Turek and Hron [2010], the experimental data of Gomes [2012] in both laminar and turbulent regimes, the validation cases and numerical results of De Nayer et al. [2014]. In this cases simple geometries were studied, almost always a plate in the wake of a bluff body such as a cylinder or a rectangle, the cases by Gomes are more complex due to the addition of a degree of freedom to the structure, namely rigid body rotation of the bluff body to which the plate is attached. Experimental results for more complex geometries (e.g. wings) exist but the fluid-structure coupling is weaker, the cases of the Aeroelastic Prediction Workshop [2012] are examples.

In this thesis the benchmarks of Turek and Hron were chosen as case studies for this FSI field since they're demanding for the codes because of the strong fluid-structure coupling but results can be obtained quickly since the geometry is 2D.

4.1 Geometry and Properties

Figure 4.1 shows the dimensions of the structure and of the computational domain, the upper and lower boundaries are walls, the flow direction is from left to right with a parabolic velocity profile imposed at the left boundary and a pressure outlet condition applied at the right boundary, the cylinder is to be treated as rigid and the plate as flexible.

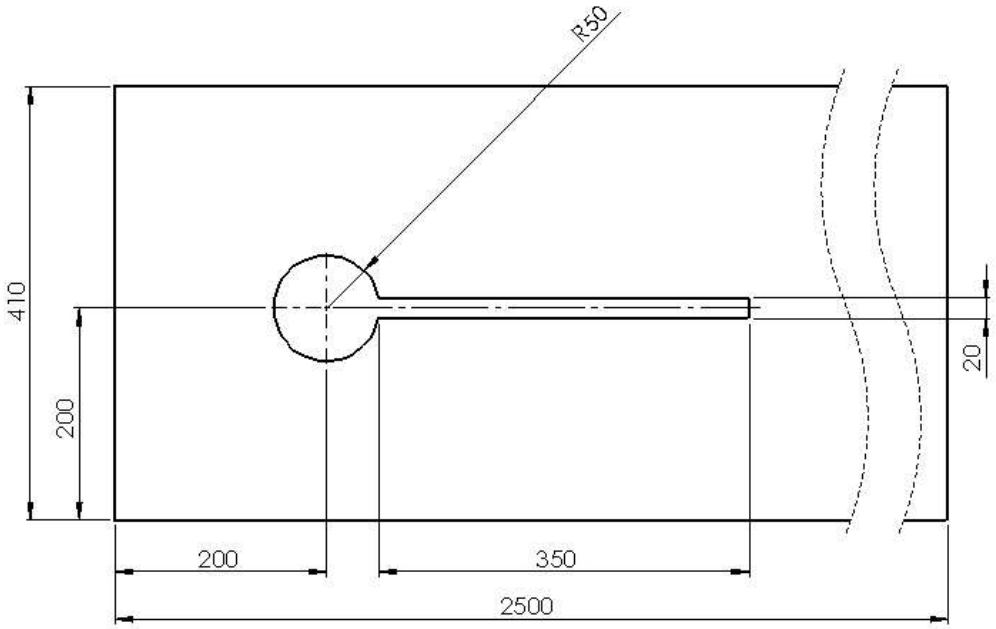

Figure 4.1 – Geometry and computational domain of the benchmarks (dimensions in mm).

The fluid and solid properties are varied to obtain different benchmark cases, the ones studied in this work are the steady and unsteady cases (properties shown in table 4.1)
The fluid is incompressible and the flow regime laminar.

Table 4.1 – Solid and fluid properties.

Benchmark	Steady	Unsteady
Fluid density [kg/m^3]	1000	1000
Dynamic viscosity [Pa.s]	0.1	1.0
Mean flow velocity [m/s]	0.2	2.0
Solid density [kg/m^3]	1000	1000
Young's modulus [MPa]	1.4	5.6
Poison coefficient	0.4	0.4

4.2 Numerical Procedure

The fluid domain was divided in the zones depicted in figure 4.2. Zone 3 is the finest and its purpose is to resolve the smaller details of the flow near the body, Zone 2 ranges from the inlet to one length (L) downstream of the plate tip, Zone 3 has length 2L. The cell size is halved from zone to zone. In zone 2 the mesh was not made coarser near the walls because the vortexes shed by the structure reach near the walls.
Prism layers were used on all walls, they are fundamental near the body's surface to accurately calculate shear stresses and pressure gradients in the normal direction.
An unstructured mesh composed of polyhedral cells was used since the gradient reconstruction method used by STAR-CCM+ works best with cells with large number of faces [v8.02 Documentation].

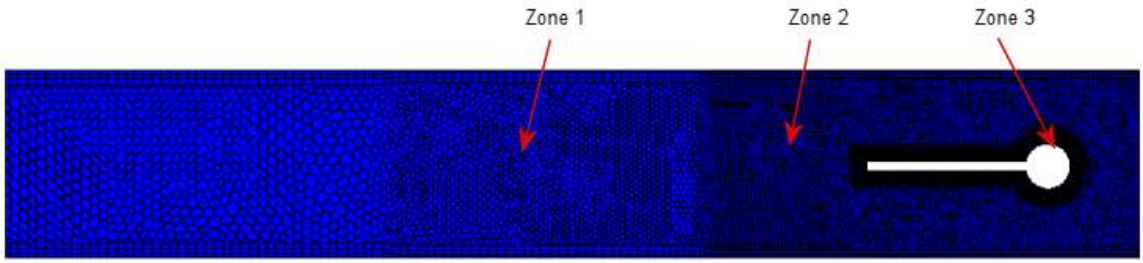

Figure 4.2 – Discretization of the computational domain.

Since the solid geometry is a simple rectangle, a cartesian mesh was used to discretize it. The elements used were 8 node linear (geometry wise, not to be confused with first order) reduced integration bricks with hourglass control (C3D8R in ABAQUS notation), because the elements are subjected to bending reduced integration avoids shear locking, the geometry has no curves and therefore quadratic elements would bring little advantage compared to the increase in computational effort.

Both meshes are 2 cell/element thick, this is necessary for the mapping algorithm between the codes to work, symmetry boundary conditions are applied at the front and back boundaries.
On the fluid side a pressure based solver was used, second order convection (second order upwind scheme) was used with the Venkatakrishnan limiter. Second order implicit time discretization was used.
Because the number of elements of the solid mesh was relatively small direct solution of the equations was used. The method for time integration is the Hilber-Hughes-Taylor method.
The implicit coupling method was used.
The parameters used in each benchmark are presented in further sections.

4.3 Solution Verification

The steady benchmark is less rich physics wise but because the equations being solved and methods being used are the same (despite having a steady state solution one has to use a time marching approach because of code limitations) it is a good verification case to assess grid convergence.

Because there's no interest in the transient behavior of the structure a number of simplification can be made to accelerate the process.

1. Large time steps.
2. First order time discretization.
3. Grid flux terms – As presented in section 2 grid flux terms arise due to the motion (morphing) of the mesh, when marching to a steady state solution they can be ignored. On the moving boundaries the grid flux from the previous time step is used, this makes convergence within the time step faster.
4. High damping – Rayleigh damping can be added to the structure to suppress transient behavior.
5. Looser coupling – Points 3 and 4 loosen the fluid-structure coupling and therefore a looser coupling strategy can be used, for example in implicit coupling data exchange can be more spaced (e.g. every 5 iterations instead of 1).

Three meshes were used to assess grid convergence, the refinement was as consistent as possible taking in consideration an unstructured mesh was used. The size of the zones of figure 4.2 was not altered. The thickness of the prism layers was maintained only the number of elements was changed, this approach was chosen because the prism layer extrusion process tends to create skewed and high aspect ratio cells near geometric discontinuities (e.g. corners), increasing the thickness leads to poorer quality cells.
From finest to coarsest the cell size on all zones was increased by a factor of 1.2, conversely the number of prism layer cells was reduced by the same factor (rounding was necessary).
The results of interest are the lift and drag forces on the whole body and the x and y displacements at

the plate's tip. Table 4.2 shows the results, number of cells, elements and mean cell size ($h=\sqrt{A/N}$ where A is the area of the computational domain) for each mesh.

Table 4.2 – Results.

Mesh	Cells	Elements	h (mm)	Drag (N/m)	Lift (N/m)	Y (mm)	X (mm)
Coarse	35216	984	5.395	14.2719	0.76523	0.82947	0.022428
Medium	48370	1372	4.603	14.2794	0.76059	0.81803	0.022859
Fine	61994	2006	4.066	14.2860	0.75864	0.81132	0.022715
Turek/Hron	19488	-	-	14.2736	0.76175	0.81930	0.022871
(monolithic)	1211392	-	-	14.2949	0.76370	0.82081	0.022716
Krafczyk	884736	-	-	14.3179	0.85491	1.01800	0.021270
(partitioned)	14155776	-	-	14.3815	0.75170	0.82010	0.022160

The first thing to note is that a constant refinement factor was not achieved, it was expected to be 1.2 and from Coarse to Medium is 1.17 and from Medium to Fine 1.13.

The x displacement values do not vary monotonically and the drag increases in a way not consistent with convergent behavior (see figure 4.3), because friction and pressure contribute equally to the drag force (see table 4.3) and the prism layer (fundamental for shear stress calculation) is the hardest area to refine consistently (integer number of cells) the deviation from the expected behavior can be explained by this.

The lift and y displacement values decrease monotonically (see figure 4.3) and the observed order of accuracy for the y displacement is 2 (as expected) and 4 for the lift, this very high value can indicate that the coarse mesh is not well inside the asymptotic range. The values obtained are within the ones reported in [Turek et al. 2010] (see table 4.2 for a sample of their results) and so it was decided not to refine the mesh further.

Table 4.3 – Contributions to the Drag force (fine mesh).

	Pressure (N)	Shear (N)	Net (N)
Cylinder	7.788	3.891	11.68
Plate	-0.2338	2.841	2.607
Total	7.554	6.732	14.29

Because for the y displacement the observed order of accuracy matches the formal order of accuracy Richardson extrapolation can be used to confidently estimate the error associated with the discretization.

$$\epsilon_h = \frac{0.81803 - 0.81132}{1.132^2 - 1} = 0.0238\,mm$$

Which represents 3% of the value calculated with the fine mesh. The same error calculation can be made for the lift force but with less confidence since the formal and observed orders of accuracy didn't

match.

$$\epsilon_h = \frac{0.76059 - 0.75864}{1.132^2 - 1} = 6.93\text{E-}3\ N$$

Or 0.9% of the value obtained with the fine mesh. Again because the observed order of accuracy was very high, 3% is a better indicator of the discretization error.

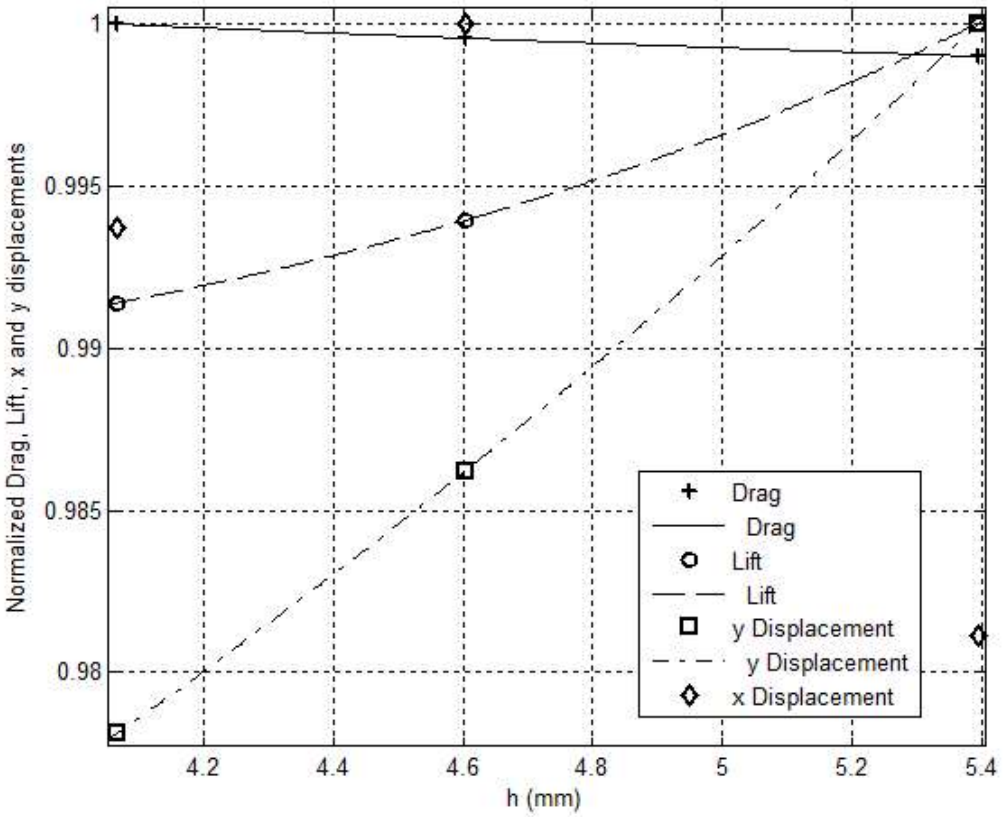

Figure 4.3 – Drag, lift, x and y displacements normalized by their maximum values.

4.4 Unsteady Case

For the unsteady benchmark the simplifications allowed by the steady case do not apply, the unsteady case was solved in the medium mesh and with a time step of 7.5E-4s, the simulations didn't ran successfully with other time steps or mesh configurations (crashed or produced non physical results), to stabilize the simulations several measures were tried, namely:

1. Ramping the forces – At the beginning of the simulation no force is applied to the body, they're increased gradually over a period of time until the full value is achieved.
2. Ramping the flow velocity – The instabilities that lead to the vibration of the structure only develop at certain flow velocities, increasing the flow velocity gradually can therefore avoid sudden changes that can be detrimental to the solution process.

3. Under-relaxation – When using the SIMPLE algorithm to solve the NS equations under-relaxation is used for pressure and velocity, in FSI its customary to relax the solid displacement i.e. in each inner iteration only part of the change in displacement is considered.
4. Low order schemes – They're usually stabler, in fact most schemes used in the discretization of the convective part of the transport equations revert to first order under certain conditions trough the use of limiters to avoid non physical solutions (e.g. wiggles).
5. Damping – Damping can be added trough the numerical method used for time integration or trough material properties. The first alternative is consistent, its effect vanishes decreasing the time step, the second is not, the problem being solved is no longer the same.

The effects each of the measures had were the following:

1. Too low of a ramping time will cause the solution to diverge, however the inverse is not true, increasing the ramping time will not stabilize the solution.
2. Ramping the flow velocity was also unsuccessful, the instabilities that lead to vibrations develop over a range of flow velocities, many structures will exhibit different vibration regimes at different velocity ranges, because the transitions between them are usually sharp sudden changes in the flow and displacement fields can occur regardless of the speed at which the velocity is varied.
3. When the under-relaxation factors being used are already quite conservative decreasing them further will only make the solution diverge slower, the end result will be the same. The divergent behavior observed was not within the inner iterations it was in the outer iterations (time steps) and therefore it was to be expected that under-relaxing would have no effect.
4. Using first order in time and in space failed. The second order schemes used in temporal discretization are implicit and the courant numbers quite small (where the cells are smallest, near the walls, the flow velocities also are, recirculation zones) and so its unlikely that the schemes were being used outside they're stability limits. First order in space had no effect probably because its was already being used locally due to the strong oscillations in the flow field.
5. Numerical damping from the Hilber-Hughes-Taylor operator (with β=0.5) was ineffective, it removed high frequency oscillations from the steady benchmark but was not enough for the unsteady one. Rayleigh damping introduces low and high frequency damping, the damping factor vs frequency curve is given by:

$$\xi = \frac{\alpha_R}{2\omega} + \frac{\beta_R \omega}{2} \tag{14}$$

Where α_R is the mass proportional coefficient (low frequency) and β_R the stiffness proportional coefficient (high frequency). β_R was chosen to give ξ=1 at 670Hz (1/2Δt) and α_R to make the damping factor at the expected frequency of vibration equal to 0.05. This was also ineffective in stabilizing the solution. Higher values were not tried because very high damping would transform the problem to the point where it would not make sense to compare the results with other authors.

As a final note on the unsuccessful tries to run the unsteady benchmark with other meshes/time steps its well known that in CFD some methods are not suited to some types of problems, for instance solving compressible flow problems with a segregated pressure based solver in some cases is not possible. In their paper Turek and Hron present more results obtained with monolithic solvers than with partitioned solvers (the category to which STAR-CCM+ / ABAQUS belong) and all of them have the linearization step mentioned in chapter 2 that the two codes used in this work lack.

The vibration of the plate is harmonic and so to characterize the values of interest (forces and displacements) the mean value, amplitude and frequency are necessary. Table 4.4 shows the results obtained in this work and a sample of the results obtained with other method [Turek et al. 2010]. Figure 4.4 shows the deformed shape of the plate at maximum tip displacement.

Table 4.4 – Results for the unsteady benchmark.

	Lift [N/m]	Y [mm]	f_y [Hz]	Drag [N/m]	X [mm]	f_x [Hz]
This work	6.34±146.5	1.34±34.7	5,352	451.7±27.3	-2.96±2.59	10.67
Turek/Hron 19488 cells 0.001 s	2.41±145.6	1.41±35.47	5.370	458.2±28.32	-3.02±2.83	10.75
Turek/Hron 304128 cells 0.00025 s	2.5±153.9	1.47±34.99	5.460	460.5±27.74	-2.88±2.72	10.93

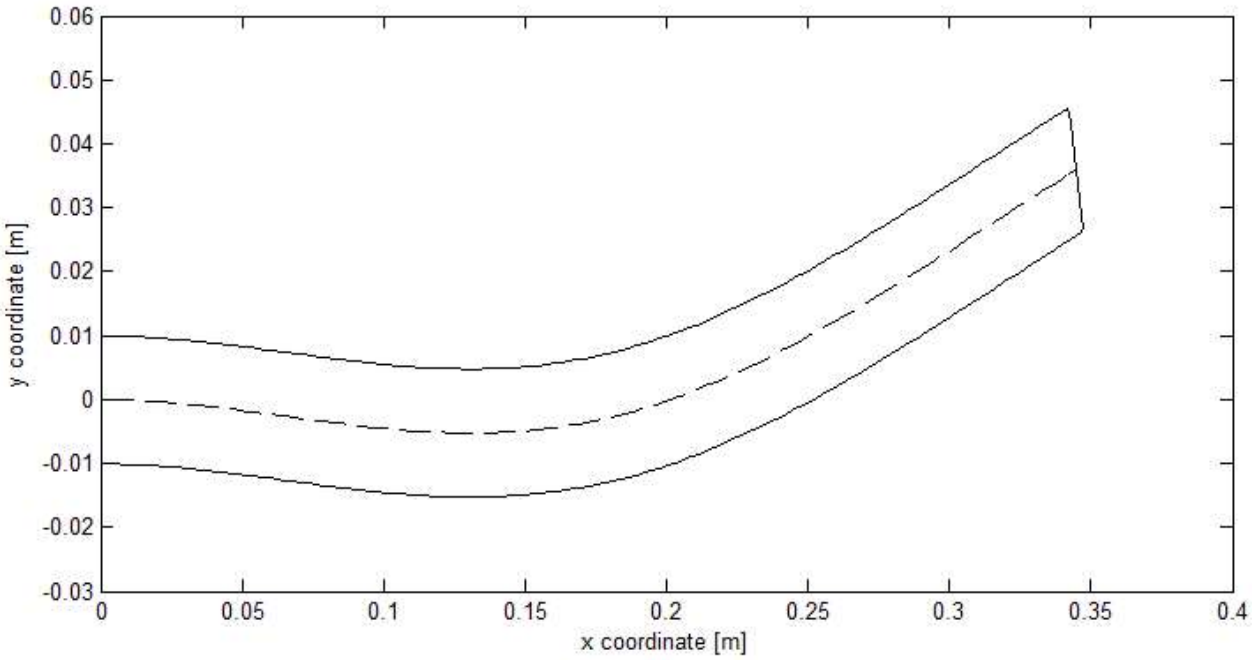

Figure 4.4 – Plate deformed shape at maximum tip displacement.

Its evident from the figure that the predominant bending mode being excited is the first, but also that it is not the only one. To further investigate this the natural modes of the plate were obtained using ABAQUS, figure 4.5 shows the deformation along the mean thickness line.

The shape functions for a cantilevered beam have the form [Pilkey, 2005]:

$$y_i(x)=\alpha_i\left[\cosh\left(\frac{\lambda_i x}{L}\right)-\cos\left(\frac{\lambda_i x}{L}\right)\right]+\beta_i\left[\sinh\left(\frac{\lambda_i x}{L}\right)-\sin\left(\frac{\lambda_i x}{L}\right)\right] \quad (15)$$

For each mode the coefficients α, β and λ were determined by fitting the expression to the data, table 4.5 shows the results.

Table 4.5 – Coefficients of the shape function for each mode.

Mode	α	β	λ	R^2
1	-1.0	-0.9797	1.313	1.0
2	0.5044	-0.5132	4.713	1.0
3	-0.5114	0.5110	7.881	1.0

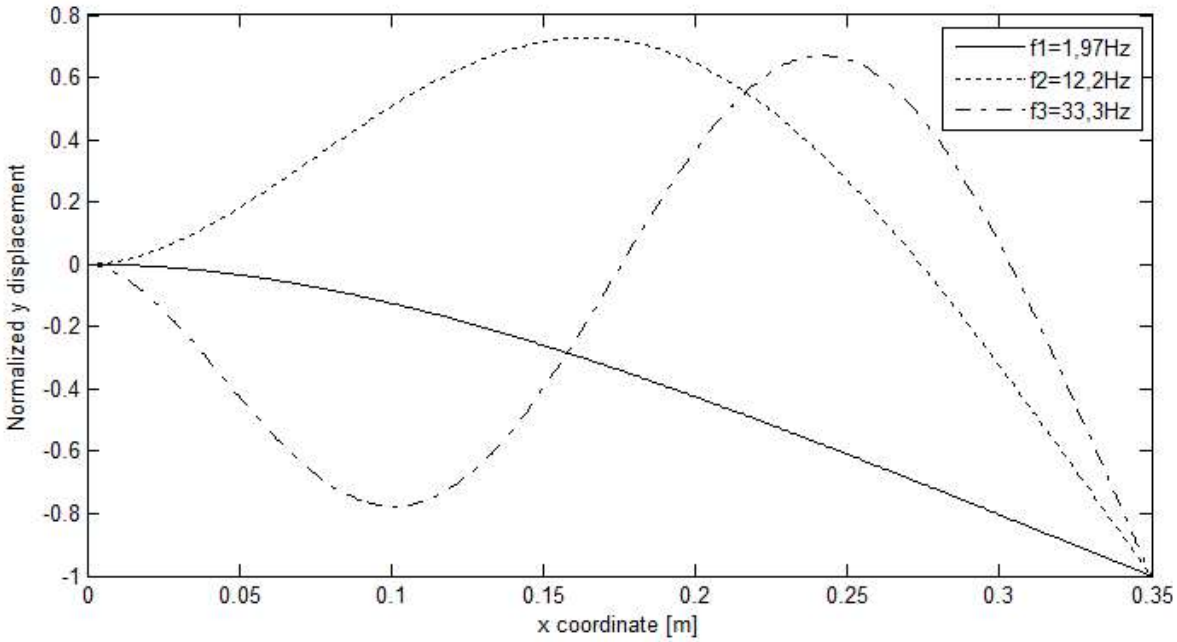

Figure 4.5 – First 3 natural modes of the plate.

The response of the plate under FSI is now expressed as a weighted sum of the natural modes plus the mean displacement ($(max(y)+min(y))/2$ for each x), the frequency however is the same for every one of them and its already known from table X.4.

$$y(x,t)=\bar{y}(x)+\sum_{1}^{\infty} y_i(x)\left(A_i\cos(\omega t)+B_i\sin(\omega t)\right) \quad (16)$$

To find coefficients A and B a surface fitting tool was used (see figure and table 4.6).

Table 4.6 – Coefficients of the surface fit.

A_1 [mm]	B_1 [mm]	A_2 [mm]	B_2 [mm]	R^2
-22.41	1.951	-11.72	-13.71	0.9997
ρ_1 [mm]	θ_1 [º]	ρ_2 [mm]	θ_2 [º]	
22.50	175.0	18.04	229.5	

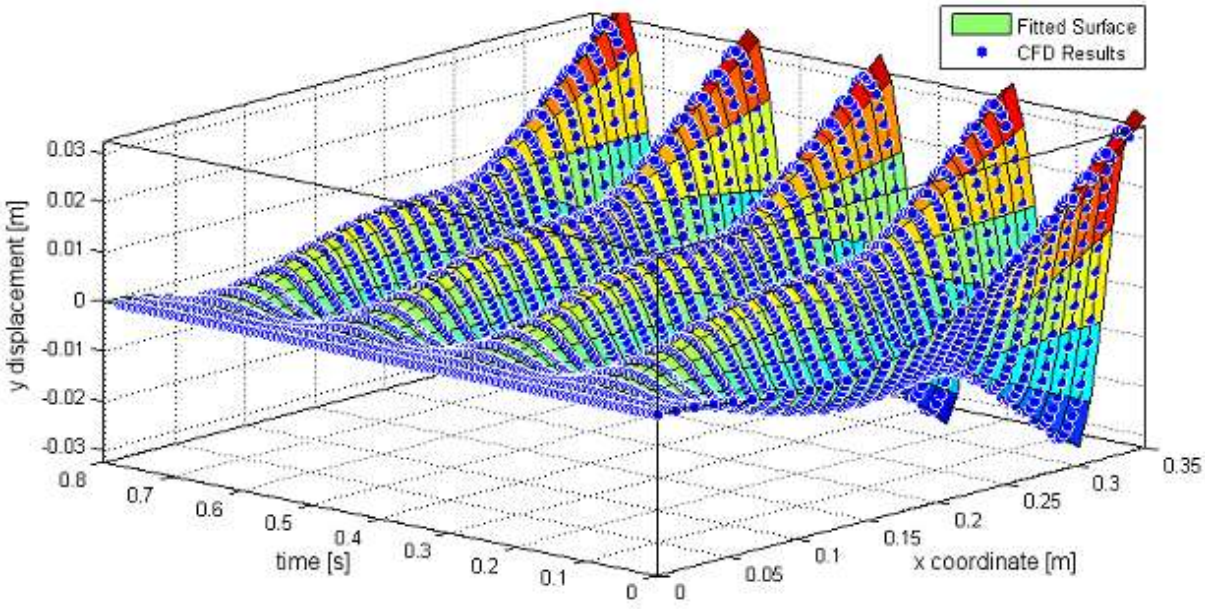

Figure 4.6 – Surface fitted to the numerical results.

The first 2 modes are the significant ones, the polar representation of the A and B coefficients shows that the first mode lags the second by 54.5º and that their magnitude is very similar (22.5 vs 18mm).
It should be noted that despite the non-linear nature of the deformation (large displacements) mode shapes determined based on linear analysis can represent it quite well.

If the plate was rigid the vortex shedding frequency would be 4.3Hz, this frequency is very far from both the first and second natural frequencies (1.97 and 12.2Hz respectively) therefore the excitation mechanism involved cannot be IIE (instability induced excitation), the vibration of the plate is caused by MIE (movement induced excitation). This excitation mechanism happens when the movement of the structure causes alterations in the flow leading to negative damping, indeed it can be observed that the lift force is almost in phase with the tip velocity (figure 4.7). They're not perfectly in phase (lift leads by 21.7º) because of the effects of added mass and stiffness.
In this case the MIE mechanism is said to involve mode coupling (because more than one natural mode is being exited) this happens when the movement from one mode produces fluid forces that transfer energy to other(s) mode(s) [Gomes, 2012]. In the case under analysis the transfer of energy is from the second to the first mode, since the former leads the latter.

Figure 4.8 shows the velocity field at different instants during a period and Figure 4.9 the pressure field, the locking in phenom can be observed, the vortex shedding is coupled with the plate motion, vortexes are shed at the extremes of tip displacement.

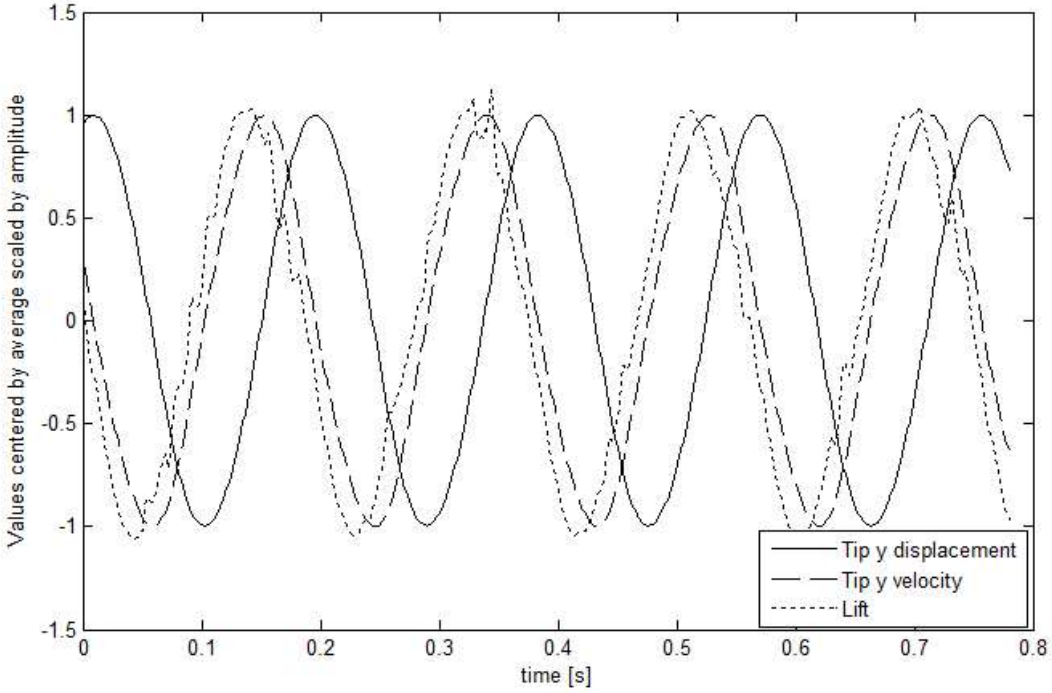

Figure 4.7 – Centered and scaled plots of tip y displacement and velocity and lift force.

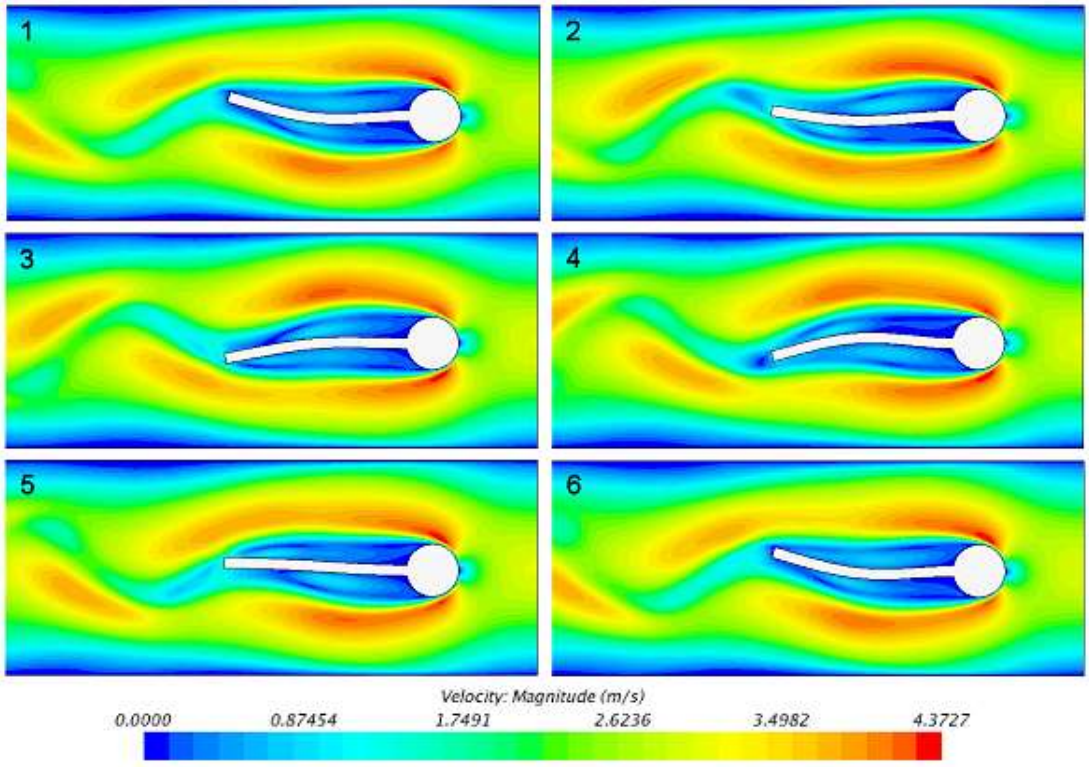

Figure 4.8 – Velocity field at different instants during a period.

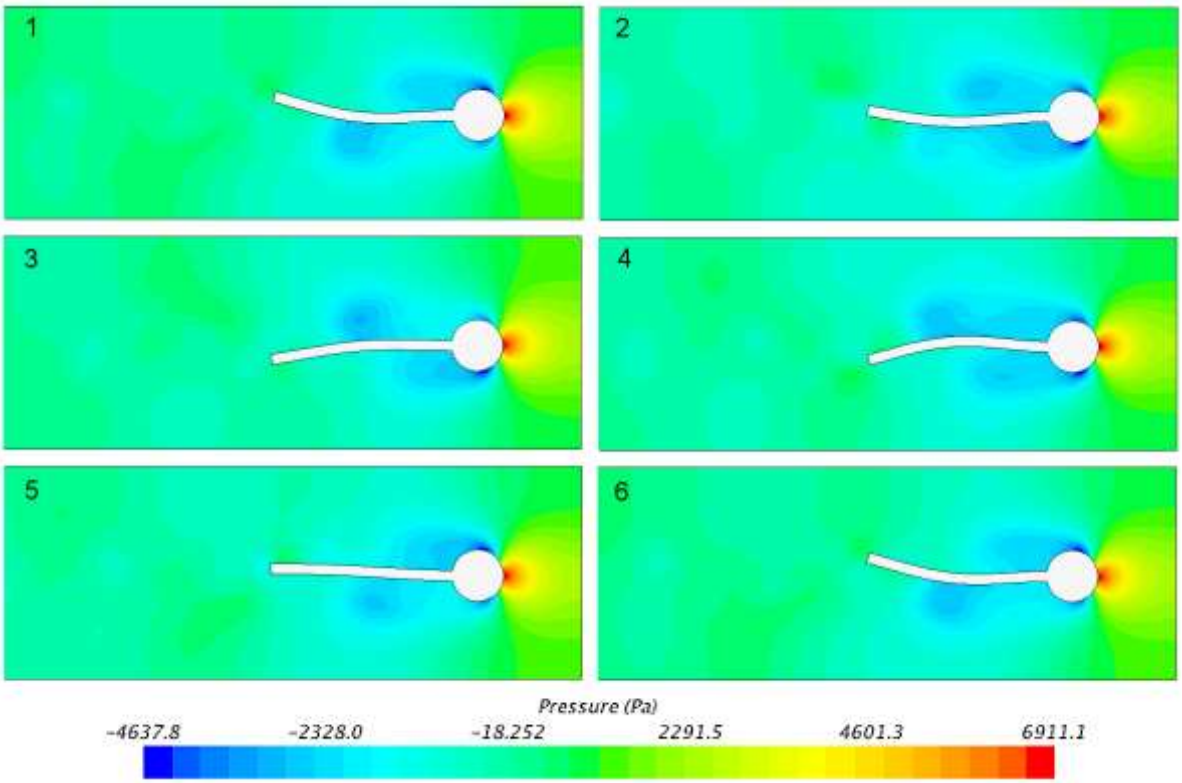

Figure 4.9 – Pressure field at different instants of a period.

5. Conclusions

Using a numerical procedure which produced results in agreement with experimental and numerical results by other authors the effects of cross-flow in the motion regimes tumbling and fluttering were studied, a wide range of cross-flow velocities was covered.

Based on the x-y trajectories as viewed from an observer moving at cross-flow velocity the hypothesis that cross-flow only affects horizontal velocity (as if the plate were a free-falling sphere in Stokes flow) was formulated.

The analysis focused on mean velocities during motion periods and their correlation, mean velocities during the trajectory, phase averaged (necessary due to cycle to cycle variations) velocities and forces during typical motion periods. Vorticity contour plots provided an explanation for the cycle to cycle variations and evidence supporting the hypothesis.

It was observed that only the horizontal velocity was changed by cross-flow and in a linear fashion. For the tumbling regime due to the large confidence bounds for the average velocities this conclusion was based on statistics (hypothesis testing), but for fluttering the motion was much more regular and so even in the trajectories the similarities are clear.

To reduce the confidence bounds for the average velocities a greater number of periods should be used, also the phase averaged velocity and pressure fields should be compared as it as been shown that the linear behavior doesn't originate from the equations. To reduce the number of cycles required for the averages the plate dimensions and/or material properties could be manipulated to produce a motion with less cycle to cycle variations.

Two FSI benchmark cases (by Turek and Hron) were solved using the commercial codes STAR-CCM+ and ABAQUS, the first which has a steady state solution was used for solution verification, forces and displacements were calculated in three meshes, convergence was checked and errors estimated to be 3% for the displacements using Richardson extrapolation. The results were compared with the ones obtained by other authors and found to be in good agreement.

For the second case, unsteady, the focus was on physics. The excitation mechanism responsible for the structure's motion was identified based on the decomposition of the structure response under FSI on its natural modes, and on the natural frequencies and frequency of the motion under FSI. Based on the difference between frequencies instability induced excitation was excluded, the excitation mechanism present is movement induced excitation with mode coupling, since more than one natural mode was needed to represent the structure's response. Again the results were compared with the ones available in the literature and were in good agreement.

The simulation of strong coupled FSI cases with STAR-CCM+ and ABAQUS although producing good results was difficult to accomplish, the success in running the simulation was more dependent on mesh and time step size than on the parameters intended to provide stability to the simulations (under-relaxation, numerical damping, etc.), in fact only one mesh/time-step combination produced results free of wiggles.

Given that both codes are “black boxes” there are not many solutions and all will have drawbacks. A solution not tried in this work is using material properties that introduce very high damping only above given strain rates. The results obtained in this way would only be reliable if the regime of very high damping was not reached.

Another is using a custom coupling algorithm that would need to be based on macros and files and therefore slow due to communication overhead, STAR-CCM+ filters the forces (by moving average) applied to bodies when simulating dynamic fluid-body interaction (DFBI in their nomenclature), such measure is not available for ABAQUS co-simulation. It's worth noting that without this filter it would be impossible to run the free-fall cases.

References

"The Aeroelastic Prediction Workshop" webpage. AIAA. https://c3.nasa.gov/dashlink/static/media/other/AEPW.htm accessed: 15/06/2014

H. R. L. Allen. "Experiments on the settling, overturning and entrainment of bivalve shells and related models". In: Sedimentology 31 (1984), pp. 227–250.

A. Andersen, U. Pesavento, and Z. Jane Wang. "Unsteady aerodynamics of fluttering and tumbling plates". In: Journal of Fluid Mechanics 541 (2005), pp. 65–90. ISSN: 1469-7645.

S.A. Ansari, R. Zbikowski, and K. Knowles. "Aerodynamic modelling of insect-like flapping flight for micro air vehicles". In: Progress in Aerospace Sciences 42.2 (2006), pp. 129–172. ISSN: 0376-0421.

A. Belmonte, H. Eisenberg, and E. Moses. "From Flutter to Tumble: Inertial Drag and Froude Similarity in Falling Paper". In: Phys. Rev. Lett. 81 (2 1998), pp. 345–348.

M. Breuer, G. De Nayer, M. Münsch. "Fluid-Structure Interaction of a Flexible Structure in a Turbulent Flow using LES." in: Direct and Large-Eddy Simulation VIII ERCOFTAC Series vol. 15 (2011) pp, 449-454.

STAR-CCM+ v8.02 Documentation. CD-adapco.

ABAQUS v6.13 Documentation. Dassault Systèmes, 2014.

G. De Nayer, A. Kalmbach, M. Breuer. "Fluid-structure interaction in turbulent flow past cylinder/plate configuration I (First swiveling mode)". ERCOFTAC. http://qnet-ercoftac.cfms.org.uk/w/index.php/UFR_2-13_Description accessed: 15/06/2014

J. Donea, A. Huerta, J.-Ph. Ponthot, A. Rodríguez-Ferran. "Arbitrary Lagrangian-Eulerian Methods." In: Encyclopedia of Computational Mechanics, Vol. 1, 2004.

P. Dupleich. Rotation in Free Fall of Rectangular Wings of Elongated Shape. Tech. Rep. 1201. NACA, 1941.

J.C. Maxwell. "On a particular case of the descent of a heavy body in a resisting medium". In: Cambridge and Dublin Mathematical Journal 9 (1854), pp. 145–148.

C. W. McCutchen. "The Spinning Rotation of Ash and Tulip Tree Samaras". In: Science 197 (1977), pp. 691–692.

S. B. Field, M. Klaus, M. G. Moore, and F. Nori. "Chaotic dynamics of falling disks". In: Nature 388 (1997), pp. 252–254.

J. Gomes. “Fluid-structure interaction-induced oscillation of flexible structures in uniform flows”. PhD thesis, Technischen Fakultat der Universitat Erlangen-Nurnberg, 2012.

K. Hirata, K. Shimizu, K. Fukuhara, K. Yamauchi, D. Kawaguchi, J. Funaki. “Aerodynamic Characteristics of a Tumbling Plate Under Free Flight”. In: Journal of Fluid Science and Technology Vol. 4 No. 1 (2009).

G. Hou, J. Wang, A. Layton. “Numerical Methods for Fluid-Structure Interaction – A Review”. In: Computational Physics Vol. 12, No. 2, pp. 337-377 (2012).

C. Jin and K. Xu. “Numerical Study of the Unsteady Aerodynamic of Freely Falling Plates”. In: Comunication in Computational Physics 3.4 (2008), pp. 834–851.

B. Kalimpa, D.M. Hargreaves, J.S. Owen. “An investigation of plate-type windborne debris flight using coupled CFD–RBD models. Part I: Model development and validation”. In: Journal of Wind Engineering and Industrial Aerodynamics no. 111 (2012) pp. 95-103.

B. Kalimpa, D.M. Hargreaves, J.S. Owen. “An investigation of plate-type windborne debris flight using coupled CFD–RBD models. Part II: Free and constrained flight”. In: Journal of Wind Engineering and Industrial Aerodynamics no. 111 (2012) pp. 104-116.

H.G. Matthies. “Strong Coupling Algorithms”. Technische Universitat Braunschweig. http://congress.cimne.com/cfsi/frontal/doc/ppt/3.pdf accessed 10/04/2014.

N.M. Newmark. “A Method of Computation for Structural Dynamics”. In: Journal of the Engineering Mechanics Division (1959).

W.L. Oberkampf, T.G. Trucano. “Verification and Validation in Computational Fluid Dynamics”. In: Progress in Aerospace Sciences (2002).

W. L. Oberkampf, C. J. Roy. “Verification and Validation in Scientific Computing”. Cambridge University Press. 2010.

U. Pesavento and Z. Jane Wang. “Falling Paper: Navier-Stokes Solutions, Model of Fluid Forces, and Center of Mass Elevation”. In: Phys. Rev. Lett. 93 (14 2004), p. 144501.

U. Pesavento. “Unsteady Aerodynamics of Falling Plates”. PhD thesis, Cornell University, 2006.

W.D. Pilkey. “Formulas for Stress Strain and Structural Matrices”. John Wiley and Sons, Inc. 2005.

N. Sardoy, J. Consalvi, B. Porterie, and A. C. Fernandez-Pello. “Modeling transport and combustion of firebrands from burning trees”. In: Combustion and Flame 150.3 (2007), pp. 151–169. ISSN: 0010-2180.

M. Souli and D. J. Benson. “Arbitrary Lagrangian Eulerian and Fluid-Structure Interaction: Numerical Simulation”. Wiley-ISTE, 2010.

Y. Tanabe, K. Kaneko. “Behavior of a Falling Paper”. In: Physical Review Letters, vol. 73 (1994), no. 10.

F. Tian, H. Dai, H. Luo, J. F. Doyle, B. Rousseau. “Fluid–structure interaction involving large deformations: 3D simulations and applications to biological systems”. In: Journall of Computational Physics 258 (2014), pp. 451-469.

S. Turek, J. Hron, M. Razzaq, H. Wobker, M. Schafer. “Numerical Benchmarking of Fluid-Structure Interaction: A comparison of different discretization and solution approaches”. 2010. http://www.mathematik.tu-dortmund.de/papers/TurekHronRazzaqWobkerSchaefer2010.pdf

K. Varshney, S. Chang, and Z. Jane Wang. “Unsteady aerodynamic forces and torques on falling parallelograms in coupled tumbling-helical motions”. In: Phys. Rev. E 87 (5 2013), p. 053021.

H. Zhong, S. Chen, C. Lee. “Experimental study of freely falling thin disks: Transition from planar zigzag to spiral”. In: Physics of Fluids 23 (2011).

N. Zorzi. “On the Uncertainty Quantification of the Unsteady Aerodynamics of 2D Free Falling Plates”. MSc thesis, IST, 2013.

A. Addition of a constant to the velocity field

In chapter 3 it was seen that cross-flow had no effect on the plate's behavior for a wide range of velocities except changing the translation velocity linearly, however the velocity field cannot change in the same way, the demonstration for that is given here.

With no cross-flow the solution of the Navier-Stokes, continuity, force and moment equilibrium equations gives a velocity field function of position and time.

$$u=u(x,y,t) \qquad v=v(x,y,t)$$

If the u velocity changed linearly with the cross-flow, c, we'd have:

$$u^{*}=u+c$$

The continuity equation is linear and therefore this new velocity field satisfies continuity. Substituting on the x momentum equation:

$$\frac{\partial u^{*}}{\partial t}+u^{*}\frac{\partial u^{*}}{\partial x}+v\frac{\partial u^{*}}{\partial y}=-\frac{1}{\rho}\frac{\partial P^{*}}{\partial x}+\nu\left(\frac{\partial^2 u^{*}}{\partial x^2}+\frac{\partial^2 u^{*}}{\partial y^2}\right)$$

$$\Leftrightarrow \frac{\partial P^{*}}{\partial x}=\frac{\partial P}{\partial x}-\rho c\frac{\partial u}{\partial x}$$

To satisfy momentum conservation a new pressure field would be necessary. The above expression for the new pressure gradient can be integrated from an arbitrary point (point A) up to a point on the plate's surface (point B), or vice versa, along the x direction to obtain the pressure distribution on the surface.

$$P_B^{*}-P_A^{*}=\int_A^B \frac{\partial P}{\partial x}-\rho c\frac{\partial u}{\partial x}dx \Leftrightarrow P_B^{*}-P_A^{*}=P_B-P_A-\rho c(u_B-u_A)$$

If point A is far from the plate and it's wake we have:

$$P_A^{*}=P_A \qquad u_A=0 \;\Rightarrow\; P_B^{*}=P_B-\rho c\,u_B$$

The only change in the forces and moment acting on the plate will be due to the term $-\rho c\,u_B$, the velocity on the surface is known because the original solution respects the no-slip condition.

$$u_B=u_{plate}-\omega_{plate}(y_B-y_{CG})$$

Where ω is the angular velocity and y_B-y_{CG} the distance along the y direction between point B and the plate's center of mass. Substituting in the expression for pressure and integrating along the plate's surface we get the variation of force per unit width:

$$\Delta F_y=-\rho h L c\omega$$

Where h is thickness and L length. Therefore for the forces to remain unchanged with cross-flow the velocity field cannot change linearly like the plate's horizontal velocity.